Development and evaluation of E3SM-MOSAIC: Spatial distributions and radiative effects of nitrate aerosol

Mingxuan Wu[1], Hailong Wang[1], Richard C. Easter[1], Zheng Lu[2], Xiaohong Liu[2], Balwinder Singh[1], Po-Lun Ma[1], Qi Tang[3], Rahul A. Zaveri[1], Ziming Ke[2], Rudong Zhang[1], Louisa K. Emmons[4], Simone Tilmes[4], Jack E. Dibb[5], Xue Zheng[3], Shaocheng Xie[3], L. Ruby Leung[1]

[1]Atmospheric Sciences and Global Change Division, Pacific Northwest National Laboratory, Richland, WA, USA
[2]Department of Atmospheric Sciences, Texas A&M University, College Station, TX, USA
[3]Lawrence Livermore National Laboratory, Livermore, CA, USA
[4]National Center for Atmospheric Research, Boulder, CO, USA
[5]Earth Systems Research Center, Institute for the Study of Earth, Oceans, and Space, University of New Hampshire, Durham, NH, USA
Correspondence to: mingxuan.wu@pnnl.gov and hailong.wang@pnnl.gov

Key Points:

- The MOSAIC module is implemented in E3SMv2 with MOZART gas chemistry to simulate nitrate aerosols
- Modeled nitrate concentrations are in good agreement with aircraft observations but have high biases at the surface
- Treatments of HNO_3 accommodation coefficients and the mixing state of dust and sea salt particles significantly impact nitrate lifecycle

Abstract

Nitrate aerosol plays an important role in affecting regional air quality as well as Earth's climate. However, it is not well represented or even neglected in many global climate models. In this study, we couple the Model for Simulating Aerosol Interactions and Chemistry (MOSAIC) module with the four-mode version of the Modal Aerosol Module (MAM4) in DOE's Energy Exascale Earth System Model version 2 (E3SMv2) to treat nitrate aerosol and its radiative effects. We find that nitrate aerosol simulated by E3SMv2-MAM4-MOSAIC is sensitive to the treatment of gaseous HNO_3 transfer to/from interstitial particles related to accommodation coefficients of HNO_3 (α_{HNO_3}) on dust and non-dust particles. We compare three different treatments of HNO_3 transfer: 1) a treatment (MTC_SLOW) that uses a low α_{HNO_3} in the mass transfer coefficient (MTC) calculation; 2) a dust-weighted MTC treatment (MTC_WGT) that uses a high α_{HNO_3} on non-dust particles; and 3) a dust-weighted MTC treatment that also splits coarse mode aerosols into the coarse dust and sea salt sub-modes in MOSAIC (MTC_SPLC). MTC_WGT and MTC_SPLC increase the global annual mean (2005-2014) nitrate burden from 0.096 (MTC_SLOW) to 0.237 and 0.185 Tg N, respectively, mostly in the coarse mode. They also produce stronger nitrate direct radiative forcing (–0.048 and –0.051 W m^{-2}, respectively) and indirect forcing (–0.33 and –0.35 W m^{-2}, respectively) than MTC_SLOW (–0.021 and –0.24 W m^{-2}). All three treatments overestimate nitrate surface concentrations compared with ground-based observations. MTC_WGT and MTC_SPLC improve the vertical profiles of nitrate concentrations against aircraft

47 measurements below 400 hPa.

48

49 **Plain Language Summary**

50 Atmospheric aerosols play an important role in the Earth's climate system through
51 their effects on radiation and clouds, and their representation continues to be a major
52 uncertainty in global climate models. Nitrate aerosol accounts for a notable fraction of
53 total aerosol mass, but it is crudely represented or even neglected in many modern global
54 climate models. In this study, we implement a comprehensive but computationally
55 efficient aerosol chemistry module in the U.S. DOE Energy Exascale Earth System
56 Model version 2 (E3SMv2), a state-of-the-science global climate model, to simulate
57 nitrate aerosols and quantify their radiative effects. Modeled nitrate concentrations are in
58 good agreement with aircraft observations but have positive biases relative to
59 ground-based network measurements. We also find that simulated nitrate lifecycle is
60 sensitive to the treatment of gaseous HNO_3 transfer to/from interstitial particles related to
61 a parameter characterizing the sticking probability of a gas molecule at the surface of
62 different aerosols such as dust and sea salt particles.

63

64

65

66

67

1. Introduction

Nitrate, formed in the atmosphere via gas-to-particle conversion of NO_x, plays an important role in the Earth's climate (Boucher et al., 2013; Naik et al., 2021). It can affect the Earth's radiation budget directly through scattering solar radiation (e.g., Adams et al., 2001; van Dorland et al., 1997) and indirectly through acting as cloud condensation nuclei (CCN) (e.g., Kulmala et al., 1993; Xu & Penner, 2012 [XP12]). The formation of nitrate aerosols can also impact the atmospheric chemistry. Ammonium nitrate forms predominantly in the fine aerosol mode through the aqueous phase reaction between HNO_3 and excess NH_3 (left after fully neutralizing sulfate) (e.g., Bassett & Seinfeld, 1983; Metzger et al., 2002). Nitrate aerosols can also form in the coarse aerosol mode through heterogeneous reactions of nitrogen species such as HNO_3 and N_2O_5 on the surface of mineral dust and sea salt particles (e.g., Chen et al., 2020; Dentener et al., 1996; Liao et al., 2003). Consequently, the consumption of HNO_3 and N_2O_5 to form nitrate aerosols reduces NO_x and further leads to a reduction of O_3 (e.g., Bauer et al., 2007 [B07]; Liao & Seinfeld, 2005; Riemer et al., 2003). More importantly, nitrate aerosols are likely to increase in the future, exerting a stronger radiative forcing (RF) on climate (e.g., Bauer et al., 2007; Bellouin et al., 2011 [B11]; Hauglustaine et al., 2014 [H14]), due to projected reductions in NO_x and SO_2 emissions but increase in NH_3 emissions in future scenarios.

Despite the important roles, nitrate aerosols are not treated in many global climate models (GCMs) participating in the Coupled Model Intercomparison Project phase 6

89 (CMIP6), which may influence the estimate of historical aerosol RF and the projection of
90 future climate change. Only a limited number of GCMs explicitly simulate the lifecycle
91 of nitrate aerosols and quantify their RF, or radiative effect (RE), due to aerosol-radiation
92 interactions (REari/RFari) (e.g., Adams et al., 2001; An et al., 2019 [A19]; Bellouin et al.,
93 2011; Bian et al., 2017 [B17]; Feng & Penner, 2007 [FP07]; Hauglustaine et al., 2014;
94 Liao et al., 2003; Lu et al., 2021 [L21]; Myhre et al., 2013; Skeie et al., 2011; Xu &
95 Penner, 2012; Zaveri et al., 2021 [Z21]; Zhou et al., 2012). Even fewer studies have
96 assessed nitrate RF/RE due to aerosol-cloud interactions (RFaci/REaci) (e.g., Lu et al.,
97 2021; Xu & Penner, 2012; Zaveri et al., 2021). B17 found that global nitrate burdens
98 from 9 GCMs participating in the Aerosol Comparisons between Observations and
99 Models (AeroCom) phase III range from 0.03 to 0.43 Tg N with a median value of 0.13
100 Tg N. Z21 summarized the simulated nitrate burdens from 12 previous studies and
101 reported a range from 0.013 to 0.52 Tg N with a median value of 0.14 Tg N. The large
102 spread in the simulated nitrate burdens results in large uncertainties in estimating nitrate
103 RFari. In AeroCom phase II experiments, global mean nitrate RFari (1850-2000) is
104 estimated to be –0.08 W m^{-2} with a range from –0.12 to –0.02 W m^{-2} (Myhre et al., 2013).
105 The Intergovernmental Panel on Climate Change (IPCC) Fifth Assessment Report (AR5)
106 gives a similar estimate of –0.11 W m^{-2} (1750-2010) but with a larger spread from –0.30
107 to –0.03 W m^{-2} (Boucher et al., 2013).

108 One key challenge in simulating the formation of nitrate aerosols is the dynamic mass
109 transfer between gas-phase HNO_3 and nitrate aerosols. Previous laboratory and field

studies found that the equilibrium timescale for submicron nitrate aerosols ranges from a few seconds (for particle diameter d_p = 0.1 μm) to around 20 minutes (for d_p = 1 μm) (Cruz et al., 2000; Dassios & Pandis, 1999; Fountoukis et al., 2009; Meng & Seinfeld, 1996), whereas it requires much longer, a few hours to days, for supermicron particles to reach equilibrium (Fridlind & Jacobson, 2000; Meng & Seinfeld, 1996). Most GCMs have adopted thermodynamic equilibrium models (TEQMs), such as ISORROPIA-I (Nenes et al., 1998), ISORROPIA-II (Fountoukis & Nenes, 2007), and EQSAM3 (Metzger & Lelieveld, 2007), to treat the gas-aerosol partitioning (e.g., Adams et al., 2001; An et al., 2019; Bauer et al., 2007; Bellouin et al., 2011; Bian et al., 2017; Hauglustaine et al., 2014; Zhou et al., 2012). FP07 used a hybrid dynamical approach (HDYN), which assumes instantaneous thermodynamic equilibrium for fine aerosols (d_p in 0.01–0.63 μm) and calculates dynamical mass transfer for coarse aerosols (d_p in 0.63–10.0 μm). They found that the HDYN approach predicts less nitrate burden, especially in the coarse mode, than the common approach (e.g., Bian et al., 2017; Fairlie et al., 2010; Hauglustaine et al., 2014) that combines a TEQM and the first-order gas-to-particle approximation to calculate the rates of heterogeneous reactions of HNO_3 onto dust and sea salt particles. Very few global modeling studies have used a fully dynamic treatment for partitioning HNO_3 over the entire aerosol size distribution (Lu et al., 2021; Zaveri et al., 2021).

The Model for Simulating Aerosol Interactions and Chemistry (MOSAIC) (Zaveri et al., 2008) is a comprehensive aerosol chemistry module. It uses the Adaptive Step

131 Time-split Euler Method (ASTEM) submodule to simulate the dynamic partitioning
132 between all semivolatile gases (HNO_3, NH_3, HCl, and secondary organic aerosol [SOA]
133 precursors) and particles of different sizes in an accurate but computationally efficient
134 way. A sectional version of MOSAIC was first implemented in the Weather Research and
135 Forecasting Model with Chemistry (WRF-Chem) (Fast et al., 2006) and applied in many
136 regional studies (e.g., Gao et al., 2014; Zhang et al., 2012). Recently, Z21 and L21
137 implemented MOSAIC in the Community Earth System Model version 1 (CESM1) and
138 version 2 (CESM2), respectively, and coupled it with the Model for Ozone and Related
139 chemical Tracers (MOZART) gas chemistry (Emmons et al., 2020) and the 7-mode and
140 4-mode version of Modal Aerosol Module (MAM7 and MAM4) (Liu et al., 2012; Liu et
141 al., 2016), respectively. The simulated concentrations of sulfate, nitrate, and ammonium
142 aerosols in CESM1 and CESM2 agree reasonably well with observations. However, they
143 used a low accommodation coefficient for HNO_3 ($\alpha_{HNO_3} \leq 0.0011$) in the
144 dust-containing MAM aerosol modes, which was measured for HNO_3 on pure dust
145 particles (Fairlie et al., 2010; Li et al., 2012). This may substantially underestimate the
146 formation of nitrate aerosols associated with gas-aerosol partitioning, particularly in the
147 MAM4 coarse mode that contains predominately sea salt over oceans, because previous
148 studies found that α_{HNO_3} on sea salt particles is much larger than the one for dust
149 particles (e.g., Abbatt & Waschewsky, 1998; Fairlie et al., 2010; Guimbaud et al., 2002;
150 Li et al., 2012; Song et al., 2007).

151 In this study, we implement MOSAIC in DOE's Energy Exascale Earth System

Model version 2 (E3SMv2) and coupled it with MAM4 (Liu et al., 2016; Wang et al., 2020) and MOZART gas-phase chemistry (Emmons et al., 2010; Tilmes et al., 2015). We also modify the calculation of mass transfer coefficients (MTCs) in MOSAIC to consider different accommodation coefficients of HNO_3 on particles that are mostly dust, partially dust, and non-dust. The goals of this study are to (1) evaluate the performance of E3SMv2-MOSAIC in simulating the spatiotemporal distributions of nitrate aerosols against ground-based observations and aircraft measurements, (2) examine the impacts of treatments of mass transfer between gaseous HNO_3 and interstitial particles on the lifecycle of nitrate aerosols due to different α_{HNO_3} on dust and non-dust particles, and (3) quantify RFari and RFaci of nitrate aerosols in E3SMv2. The paper is organized as follows. Section 2 describes the calculation of MTCs, accommodation coefficients, the coupling between MOSAIC and MAM4/MOZART in E3SMv2, and the model experiments design. Section 3 shows the changes of nitrate mass budgets due to different MTC treatments, evaluates modeled nitrate concentrations against ground-based observations and aircraft measurements, and then gives the estimation of RFari and RFaci of nitrate aerosols. Discussion and conclusions are presented in Section 4.

2. Methodology

2.1. Model Description

In this study, we use E3SMv2 (Golaz et al., 2022) along with its atmosphere component (EAMv2) and land component (ELMv2). Compared to EAMv1 (Rasch et al.,

2019; Xie et al., 2018), the deep convection scheme (ZM, Zhang & McFarlane, 1995) in EAMv2 adopts the dynamic Convective Available Potential Energy (dCAPE) trigger (Xie & Zhang, 2000) and an unrestricted air parcel launch level (ULL) approach (Wang et al., 2015), which improves the simulated precipitation (Xie et al., 2019), particularly the precipitation diurnal cycle. EAMv2 mostly adopts most of the tunable parameters in the parameterizations of (1) turbulence, cloud macrophysics, and shallow convection (CLUBB, Golaz et al., 2002; Bogenschutz et al., 2013), (2) deep convection, and (3) cloud microphysics (MG2, Gettelman & Morrison, 2015) from the recalibrated atmosphere model, EAMv1P, which significantly improves the simulations of clouds and precipitation climatology (Ma et al., 2022). The high equilibrium climate sensitivity (ECS = 5.3 K) in E3SMv1 is also reduced to 4 K in E3SMv2.

In MAM4 of EAMv2 (Liu et al., 2016; Wang et al., 2020), mass and number mixing ratios of aerosol species, including black carbon (BC), primary organic matter (POM), SOA, marine organic aerosol (MOA), sulfate, mineral dust, sea salt and aerosol water, in four lognormal modes are predicted with a prescribed geometric standard deviation for each mode. Aerosol particles are assumed to be internally mixed within the same mode and externally mixed between different modes. Compared to EAMv1, EAMv2 changes the size distribution of emitted dust particles following the brittle fragmentation theory (Kok, 2011) with prescribed mass fraction of 1.1% and 98.9% for the accumulation and coarse modes, respectively.

194 **2.2. The Coupling between MOSAIC and MAM4/MOZART**

195 To couple MOSAIC with MAM4 in EAMv2, we add additional aerosol species in
196 MAM4 following L21. As listed in Table 1, we add nitrate aerosol (NO_3^-) to the
197 accumulation, Aitken, and coarse modes to simulate the formation of various salts
198 containing nitrate anions (e.g., NH_4NO_3, $NaNO_3$, and $Ca(NO_3)_2$) in MOSAIC. Note that
199 nitrate and other secondary species are allowed to form on the primary carbon mode
200 particles, but they are immediately transferred to the accumulation mode though the
201 aging process. The optical properties (e.g., refractive index) of nitrate aerosols are set to
202 those of sulfate. We use 0.67 for the hygroscopicity of nitrate aerosols (Petters &
203 Kreidenweis, 2007) following L21 and XP12, which is larger than the hygroscopicity of
204 sulfate aerosols. Same as nitrate aerosol, ammonium aerosol (NH_4^+) is added to the three
205 MAM4 modes to simulate the formation of various salts containing ammonium cations
206 (e.g., NH_4NO_3, NH_4HSO_4, and NH_4Cl). Sulfate aerosol represents SO_4^{2-} when MOSAIC
207 is coupled with MAM4, while it represents NH_4HSO_4 in the default MAM4.

208 MOSAIC explicitly treats the heterogeneous reactions of HNO_3 on dust (i.e., $CaCO_3$)
209 and sea salt (i.e., NaCl) particles. To consider the reactions on dust in MAM4, we add
210 calcium (Ca^{2+}) and carbonate (CO_3^{2-}) aerosols in each mode containing dust with emitted
211 mass fractions of 2% and 3%, respectively, following Zaveri et al. (2008). The remaining
212 95% of the emitted dust in each mode is treated as other inorganic (OIN) in MOSAIC,
213 which does not have chemical reactions with gas and aerosol species. In the default
214 MAM4 of EAMv2, dust is only present in the accumulation and coarse modes. When we

initially coupled MOSAIC with the default MAM4 in E3SM, we found that the model yielded much stronger REaci (~ −1.0 W m^{-2}) than L21. This was found to be due to strong production of nitrate aerosols in the Aitken mode caused by using a much higher α_{HNO_3} (0.65) for the Aitken mode but lower values (≤0.0011) for the accumulation and coarse modes in the calculation of MTCs. We discuss this issue in detail in section 2.3. We then add dust species (OIN, calcium, and carbonate) to the Aitken mode (0.00165% of the total dust mass emission) to avoid too strong REaci and be consistent with the configuration of L21. As in Z21 and L21, primary sea salt aerosol in each MAM4 mode is split into three species: sodium (Na^+), chloride (Cl^-), and sea salt sulfate, with emitted mass fractions of 38.5%, 53.8%, and 7.7%, respectively.

MOSAIC implemented in EAMv2 replaces the default MAM4 treatment of gas-aerosol exchange and simulates the dynamic mass transfer between semivolatile gases, including H_2SO_4, HNO3, HCl, NH_3, and a single lumped SOA precursor, and aerosols, including sulfate, nitrate, ammonium, chloride, and SOA. The aqueous (i.e., cloud water) chemistry, which already includes reactions of SO_2, is also modified to include reactions of HNO_3, NH_3, and HCl. MOSAIC is coupled with MOZART-4 gas chemistry scheme (Emmons et al., 2010; Tilmes et al., 2015) that predicts HNO_3 through O_3-NO_x-HO_x chemistry or N_2O_5 hydrolysis. Nighttime nitrate radical (NO_3) oxidation of biogenic volatile organic compounds (BVOC) can lead to the formation of appreciable amount of SOA composed of organic nitrates (e.g., Fisher et al., 2016; Hao et al., 2014; Kiendler-Scharr et al., 2016; Ng et al., 2017; Rollins et al., 2012; Zaveri et al., 2010;

Zaveri et al., 2020). Although about 10% of the global mean SOA burden was estimated to form via NO_3-BVOC chemistry (Pye et al., 2010), the fate and importance of particle-phase organic nitrates are still uncertain due to its poorly constrained sinks such as hydrolysis to HNO_3 (Pye et al., 2015). Consequently, formation of particulate organic nitrates is not presently treated by MOSAIC but will be considered in the future. Note that we have also removed some coding bugs in the coupling between MOSAIC and parameterizations of cloud microphysics (e.g., mixed-phase cloud ice nucleation) in EAMv2, compared to Z21 and L21, and an error in the implementation of the wet deposition scheme (Neu & Prather, 2012) that affects the removal rates of weakly soluble species.

2.3. Mass Transfer Coefficients and Accommodation Coefficients

In MOSAIC, the dynamic mass transfer equations for gases to/from interstitial aerosol particles are expressed as:

$$\frac{dC_{a,i,m}}{dt} = k_{j,m}\left(C_{g,j} - C_{eq,j,m}\right) \quad (1)$$

$$\frac{dC_{g,j}}{dt} = -\sum_m k_{j,m}\left(C_{g,j} - C_{eq,j,m}\right) \quad (2)$$

where $C_{a,i,m}$ (nmol m^{-3}) is the concentration of aerosol species i in aerosol mode m; $C_{g,j}$ (nmol m^{-3}) is the concentration of gas species j; $C_{eq,j,m}$ is the equilibrium concentration of gas species j on the particle surface in mode m; and $k_{j,m}$ (s^{-1}) is the MTC. The MTC (k_j) for a single particle size (r_p) can be calculated as:

$$k_j = 4\pi r_p D_{g,j} n(r_p) f\left(Kn_j(r_p), \alpha_j\right) \quad (3)$$

where r_p is the particle radius; $D_{g,j}$ is the gas diffusivity of specie j; n is the number concentration of particles; and $f(Kn_j, \alpha_j)$ is the transition regime correction factor (Fuchs & Sutugin, 1971) as a function of the Knudsen Number Kn_j and accommodation coefficient α_j. Equation (3) is integrated (averaged) over each mode's lognormal size distribution to obtain $k_{j,m}$. $f(Kn_j, \alpha_j)$ is calculated as:

$$f(Kn_j, \alpha_j) = \frac{0.75\alpha_j(1+Kn_j)}{Kn_j(1+Kn_j)+0.283\alpha_j Kn_j+0.75\alpha_j} \quad (4)$$

The accommodation coefficient represents the sticking probability of a gas molecule at the particle surface (Feng & Penner, 2007). It is a key parameter in calculating dynamic mass transfer. If α_j increases, $k_{j,m}$ would increase and may further lead to an increase in aerosol concentrations.

When Z21 implemented MOSAIC in CESM1, they introduced a relatively low α_{HNO_3} (≤0.0011) for HNO_3 onto dust particles (i.e., dust containing aerosol modes), which is calculated as a function of relative humidity (RH):

$$\alpha = \begin{cases} \frac{0.0018RH}{(1-RH)(1+7RH)} & RH<0.8 \\ 0.0011 & RH\geq 0.8 \end{cases} \quad (5)$$

The formula follows Li et al. (2012) but is modified to match the uptake coefficients from Fairlie et al. (2010). This low α was also used for HCl onto dust containing modes. A much higher value ($\alpha_{HNO_3} = 0.65$) was used for HNO_3 and HCl onto modes that do not contain any dust. In the CESM1-MAM7 initially used by Z21, dust was only present in the fine and coarse dust modes, as in Liu et al. (2012). Z21 later switched to a newer version of CESM1, in which dust is present in the Aitken and accumulation modes (in

277 relatively small amounts). An unplanned side effect of this switch was that equation (5)
278 was applied to the Aitken and accumulation modes, as they always contained non-zero
279 (although often extremely small) amount of dust species. When L21 implemented
280 MOSAIC in CESM2-MAM4 (using the code from CESM1-MAM7), equation (5) was
281 likewise applied for the accumulation, Aitken, and coarse modes of MAM4 everywhere,
282 even at locations where dust concentrations were minor. Equation (5) was derived and
283 calibrated for HNO_3 on pure dust particles, and α_{HNO_3} for aerosol species, such as sea
284 salt and nitrate, are much larger than that for pure dust (e.g., Abbatt & Waschewsky, 1998;
285 Dassios & Pandis, 1999; Fairlie et al., 2010; Guimbaud et al., 2002; Li et al., 2012; Song
286 et al., 2007). Thus equation (5) should probably only be used for modes that are
287 predominately dust at certain location and time. Note that while MAM assumes that
288 aerosols in each mode are internally mixed, dust particles are often externally mixed with
289 other types of particles (e.g., sea salt) in the real world. This should be considered for
290 HNO_3 mass transfer to/from particles. It should also be noted that equation (5) is not used
291 in MOSAIC of WRF-Chem.

292 To account for the different accommodation coefficients of HNO_3 on dust and
293 non-dust particles, we first introduce a dust-weighted MTC treatment. Within the
294 MOSAIC routine that calculates MTCs, we temporarily divide each aerosol mode into
295 dust and non-dust sub-modes. The dust sub-mode only contains dust species, and the
296 number concentrations ($n_{dst,m}$) are calculated using prescribed typical mass median
297 diameters ($r_{dst,p,m}$) of 0.089, 0.52, and 2.626 μm (summarized from values over dust

298 regions) for the Aitken, accumulation, and coarse modes, respectively. The non-dust
299 sub-mode contains the other aerosol species and the remaining number concentrations
300 ($n_{ndst,m} = n_m - n_{dst,m}$). We calculate an MTC for each sub-mode, using equation (5) for the
301 dust sub-mode and $\alpha_{HNO_3} = 0.193$ (following FP07 and XP12) for the non-dust
302 sub-mode. The MTCs for the two sub-modes are then added to form a total MTC for an
303 aerosol mode in MAM4. With this treatment, the other parts of the MOSAIC module are
304 unaware of the sub-modes.

305 Aerosol nitrate formation is strongly dependent on particle composition. Z21 found
306 that most of the nitrate mass (~73% of the total annual burden) exists in the fine and
307 coarse sea salt modes of MAM7. Nitrate burden in the coarse sea salt mode (0.57 mg m^{-2})
308 was much larger than the one in the coarse dust mode (0.06 mg m^{-2}). We make a step
309 further by modifying the dust-weighted MTC treatment to split the aerosols in the coarse
310 mode of the default MAM4 into the coarse dust and coarse sea salt sub-modes before
311 calling MOSAIC module, so that MOSAIC works with 5 aerosol modes. We apply
312 equation (5) to calculate α_{HNO_3} in the coarse dust sub-mode and $\alpha_{HNO_3} = 0.193$ in the
313 coarse sea salt sub-mode. We first partition aerosol number concentrations in the coarse
314 mode into the two sub-modes, using prescribed typical mass median diameters for pure
315 dust (2.626 μm) and sea salt (2.059 μm) particles as well as mass concentrations of
316 primary dust (OIN/0.95) and primary sea salt (sodium/0.385). Mass concentrations of
317 OIN, calcium, and carbonate are assigned to the coarse dust sub-mode, while mass
318 concentrations of sodium, sea salt sulfate, and MOA are assigned to the coarse sea salt

sub-mode. The mass fractions of nitrate and ammonium partitioned to the coarse sea salt sub-mode are calculated using fitting relations, $y = x^a$ (a = 0.11 and 0.01, respectively) where x is the mass fraction of primary sea salt to the sum of coarse mode primary sea salt and dust. The mass fraction of non-sea-salt sulfate (nss-sulfate) partitioned to the coarse dust sub-mode is calculated using $y = x^{0.18}$ where x is the mass fraction of primary dust to the sum of coarse mode primary sea salt and dust. These fitting relations are derived from the simulations of Z21 that used MAM7 which treats dust and sea salt in separate modes (fine/coarse dust modes and fine/coarse sea salt modes). BC, POM, and SOA are partitioned using number fractions of aerosol number concentrations in the sub-modes to the total coarse mode number concentrations. After 11 of the 12 aerosol species in the coarse mode have been partitioned, chloride is partitioned so that the two sub-modes have equal normalized charge balance (i.e., (cations – anions)/(cations + anions)). Finally, dry and wet mass median diameters are calculated using the partitioned aerosol mass and number concentrations. After all calculations in MOSAIC are done within the model time step, coarse mode aerosol mass and number concentrations are updated to the sum of values from the two sub-modes. This mode splitting is admittedly highly approximate, but it does allow MOSAIC to treat the different heterogeneous reactions of HNO_3 onto dust and sea salt particles.

2.4. Experiments Design

We ran E3SMv2 with the spectral-element dynamical core for EAMv2 at

approximately 1-degree horizontal resolution (ne30pg2) with 72 vertical layers from 2004 to 2014, and the last 10-yr results are used for our analysis. The horizontal wind components u and v were nudged towards the Modern-Era Retrospective analysis for Research and Applications Version 2 (MERRA-2) (Gelaro et al., 2017) meteorology using a relaxation timescale of 6 h to facilitate the evaluation of MOSAIC against observations under realistic meteorological conditions. Monthly mean prescribed historical SST and sea ice in 2004-2014 were used. We used the anthropogenic and biomass burning emissions of aerosols and precursor gases specified for CMIP6 (Hoesly et al., 2018; van Marle et al., 2017), except for SOA precursors (Wang et al., 2020). Biogenic emissions were calculated online using the Model of Emissions of Gases and Aerosols from Nature version 2.1 (MEGANv2.1) (Guenther et al., 2012) incorporated in ELMv2.

As summarized in Table 2, we conducted five sets of experiments with present-day (PD, 2005-2014) and preindustrial (PI, 1850) emissions of aerosols and precursor gases. In MTC_SLOW, MTC_WGT, and MTC_SPLC, we ran E3SMv2-MOSAIC with and without the formation of nitrate aerosols. Note that MOSAIC module is still active when HNO_3 partitioning to particles is turned off. In MTC_SLOW, MOSAIC was coupled with MOZART and MAM4 in a way following L21. Equation (5) was used to calculate α_{HNO_3} and α_{HCl} in the accumulation, Aitken, and coarse modes, which has a maximum value of 0.0011. In MTC_WGT, we applied the dust-weighted MTC treatment introduced in section 2.3. Equation (5) was used to calculate α_{HNO_3} and α_{HCl} on dust particles,

361 while $\alpha_{HNO_3} = 0.193$ and $\alpha_{HCl} = 0.1$ were used for non-dust particles. In MTC_SPLC,
362 as introduced in section 2.3, we still adopted the dust-weighted MTC treatment in the
363 accumulation and Aitken modes but split coarse mode aerosols into the coarse dust and
364 sea salt sub-modes in MOSAIC. Equation (5) was used to calculate α_{HNO_3} and α_{HCl} in
365 the coarse dust sub-mode, while $\alpha_{HNO_3} = 0.193$ and $\alpha_{HCl} = 0.1$ were used in the
366 coarse sea salt sub-mode. Note that we used $\alpha_{NH_3} = 0.65$ in MTC_SLOW and
367 $\alpha_{NH_3} = 0.092$ (Feng & Penner, 2007; Xu & Penner, 2012) in MTC_WGT and
368 MTC_SPLC. In sections 3.1-3.4, we focus on the experiments with the formation of
369 nitrate turned on and PD emissions of aerosols and precursor gases (i.e.,
370 MTC_SLOW_PD, MTC_WGT_PD, and MTC_SPLC_PD). In section 3.5, we use the
371 experiments with the formation of nitrate turned off and/or PI emissions (i.e.,
372 xx_PD_noNO3, xx_PI, and xx_PI_noNO3) to estimate RFaci/REaci of nitrate aerosols
373 following Ghan (2013). Default and MZT mentioned in section 3.1 are meant for
374 experiments with PD emissions. Note that we also conducted an experiment that further
375 splits accumulation mode aerosols into three sub-modes in MOSAIC (MTC_SPLAC) and
376 an experiment that used $\alpha_{HNO_3} = 0.193$ for all MAM4 modes (MTC_FAST). As shown
377 in Table S1, MTC_SPLAC gives similar nitrate burden to MTC_SPLC (0.191 versus
378 0.185 Tg N). MTC_FAST produces slightly larger burden than MTC_WGT (0.256 versus
379 0.237 Tg N).
380

381 **2.5. Observations**

382 We first validate profiles of key gas species, including O_3, CO, NO_x, peroxyacetyl
383 nitrate (PAN) and HNO_3, against the averaged profiles, derived by Tilmes et al. (2015),
384 from various aircraft campaigns between 1995 and 2010 for different regions and seasons
385 around the globe. Modeled tropospheric column ozone (TCO) is evaluated against
386 satellite retrievals from the Ozone Monitoring Instrument (OMI) and the Microwave
387 Limb Sounder (MLS) onboard Aura (Ziemke et al., 2006), the same data used by Tang et
388 al. (2021) to evaluate E3SMv1/v2. To evaluate surface mass concentrations of modeled
389 precursor gases (HNO_3, NH_3, and SO_2) and aerosols (nitrate, ammonium, and sulfate), we
390 use ground-based observations from the Clean Air Status and Trends Network
391 (CASTNET) and the Ammonia Monitoring Network (AMoN) over U.S., the European
392 Monitoring and Evaluation Programme (EMEP) over Europe, and the Acid Deposition
393 Monitoring Network in East Asia (EANET) over East Asia. To better understand the
394 model biases of surface HNO_3, we compare modeled surface NO_x with ground-based
395 observations from U.S. EPA Air Quality System (AQS), EMEP, and EANET. We also
396 compare modeled vertical profiles of aerosols with measurements from the Soluble
397 Acidic Gases and Aerosol (SAGA) filters during aircraft campaigns, including the
398 Intercontinental Chemical Transport Experiment Phase B (INTEX-B) (Singh et al., 2009),
399 Arctic Research of the Composition of the Troposphere from Aircraft and Satellites
400 (ARCTAS) (Jacob et al., 2010), Deep Convective Clouds and Chemistry (DC3) (Barth et
401 al., 2015), Studies of Emissions and Atmospheric Composition, Clouds, and Climate
402 Coupling by Regional Surveys ($SEAC^4RS$) (Toon et al., 2016), and Atmospheric

403 Tomography Mission (ATom) (Thompson et al., 2021). A cutoff size of d_p = 4 μm is
404 applied to modeled profiles of aerosols for comparison (i.e., PM_4), as the collection
405 efficiency of SAGA filters' inlet reduces to 50% for aerosols with d_p around 4 μm (Guo et
406 al., 2021; McNaughton et al., 2007).
407
408 **3. Results**
409 **3.1. Evaluation of Key Gas Species**
410 In Figure 1, we first evaluate modeled tropospheric (2-7 km) gases from MZT and
411 MTC_SLOW (2005-2014) against the summarized observations from aircraft campaigns
412 (1995-2010) for different regions (Southern Hemisphere [SH], Tropics, Northern
413 Hemisphere [NH] mid-latitudes, and NH Polar) and seasons (March-April-May [MAM],
414 June-July-August [JJA], September-October-November [SON], and
415 December-January-February [DJF]). Simulated O_3 concentrations have a very good
416 agreement with aircraft observations. However, simulated TCO has significant low biases
417 in the SH compared with OMI/MLS (Figure S1), which is similar to CESM1.2 (Tilmes et
418 al., 2015) and may be caused by the underestimation of biomass burning emissions (e.g.,
419 CO and VOCs). Modeled CO concentrations agree with the observations fairly well in
420 the SH and Tropics but have significant low biases in the NH mid- and high latitudes,
421 particularly in DJF and MAM, likely due to missing sources of anthropogenic emissions
422 (Emmons et al., 2020). MZT and MTC_SLOW underestimate NO_x but tend to
423 overestimate HNO_3 in the NH mid- and high latitudes, which may be caused by too fast

chemical conversion from NO_x to HNO_3 or missing sources of NO_x emissions. Simulated concentrations of O_3, CO, NO_x, and PAN are quite close between MZT, MTC_SLOW, MTC_WGT, and MTC_SPLC (not shown). MTC_SLOW produces notably lower HNO_3 than MZT, especially in the NH mid- and high latitudes, due to the neglected formation of nitrate aerosols in MZT. In general, EAMv2 with MOZART and MOSAIC performs similarly as CESM1.2 (Tilmes et al., 2015), the Community Atmosphere Model Version 6 with interactive chemistry (CAM6-chem) (Emmons et al., 2020), and Z21, in simulating tropospheric gases (also see Figure S2).

3.2. Mass Budgets and Spatial Distributions of Nitrate and Other Aerosol Species

In this section, we examine the changes in mass budgets and spatial distributions of nitrate and other aerosol species due to different treatments in calculating MTCs. As shown in Table 3, global annual mean nitrate burden significantly increases from 0.096 (MTC_SLOW) to 0.237 (MTC_WGT) and 0.185 Tg N (MTC_SPLC), and there are large increases in both fine and coarse mode nitrate burdens. For the increase in coarse mode nitrate burden, it is primarily due to the increase in gas-aerosol exchange production, as aqueous chemistry production is negligible and gas-aerosol exchange loss is relatively small. The MTC treatments considering high α_{HNO_3} on non-dust particles in MTC_WGT and MTC_SPLC substantially increase the net production of coarse mode nitrate from 6.4 (MTC_SLOW) to 16.0 and 12.9 Tg N a^{-1}, respectively, through gas-aerosol exchange. For fine mode nitrate, the net chemical production is determined

445 by both large aqueous chemistry production and strong net loss through gas-aerosol
446 exchange. The strong gas-aerosol exchange loss of fine mode nitrate (–54.9 to –51.4 Tg
447 N a^{-1}) leads to net loss through gas-aerosol exchange (–30.5 to –20.8 Tg N a^{-1}). The
448 increase in fine mode nitrate burden is due to two factors. First, the MTC treatments in
449 MTC_WGT and MTC_SPLC increase the net production of fine mode nitrate from 6.4
450 (MTC_SLOW) to 7.7 and 8.2 Tg N a^{-1}, respectively, because of the reduction in the net
451 loss through gas-aerosol exchange. Second, MTC_WGT and MTC_SPLC have lower
452 mass fractions of cloud-borne nitrate for the fine mode. It contributes to longer lifetime of
453 fine mode nitrate in MTC_WGT and MTC_SPLC, because cloud-borne nitrate aerosols
454 have much shorter lifetime than the interstitial ones due to strong wet removal.

455 Compared with MTC_WGT, the net production of coarse mode nitrate through
456 gas-aerosol exchange in MTC_SPLC decreases from 16.0 to 12.9 Tg N a^{-1} due to the
457 treatment of splitting the coarse mode in MOSAIC. In MTC_SPLC, coarse dust and sea
458 salt particles are externally mixed with low (≤0.0011) and high (0.65) α_{HNO_3},
459 respectively, in MOSAIC. To compensate for the reduction in coarse mode production,
460 the net production of fine mode nitrate in MTC_SPLC increases from 7.7 to 8.2 Tg N a^{-1}.
461 Consequently, the fine mode nitrate burden increases from 0.068 (MTC_WGT) to 0.076
462 Tg N (MTC_SPLC), while the coarse mode nitrate burden decreases from 0.169 to 0.110
463 Tg N. In contrast to the large increase of nitrate burdens in MTC_WGT and MTC_SPLC,
464 we find only a slight increase of ammonium burden from 0.390 to 0.430 and 0.436 Tg N.
465 This indicates that the increase in the formation of $NaNO_3$ and $Ca(NO_3)_2$ through

466 heterogeneous reactions with dust and sea salt mainly contributes to the increase of
467 nitrate burdens in MTC_WGT and MTC_SPLC. The differences in nss-sulfate burdens
468 among MZT, MTC_SLOW, MTC_WGT, and MTC_SPLC are quite small (within 1%,
469 see Table S2). The Default experiment has slightly higher nss-sulfate burden (0.784 Tg S)
470 than the other four experiments (ranging from 0.702 to 0.706 Tg S) due to larger
471 chemical production related to higher O_3 concentrations.

472 As shown in Figures 2a–2c, large values of nitrate burden are in East Asia, India,
473 Europe, and northeastern U.S. due to high anthropogenic emissions of NO_x and NH_3 and
474 in equatorial Africa due to high biomass burning emissions. These are mainly contributed
475 by fine mode nitrate (accumulation and Aitken mode), while coarse mode nitrate mainly
476 contributes to the total burden over oceans and dust source regions (Figure 3). Compared
477 to MTC_SLOW, nitrate burdens in MTC_WGT and MTC_SPLC increase around the
478 globe. In Figure 2b, large increases are found over regions with high anthropogenic or
479 biomass burning emissions of NO_x, resulting from the substantial reduction in net loss of
480 fine mode nitrate through gas-aerosol exchange in MTC_WGT (Figure S3). We also see
481 large increases in nitrate burden over dust source regions (Middle East, Sahel, and
482 northwestern China) associated with the increase in net production of coarse mode nitrate
483 through gas-aerosol exchange (Figure S3). Compared to MTC_WGT, MTC_SPLC has a
484 smaller increase of nitrate burden globally, especially in dust source regions (Figures 2c
485 and 2f). There are also large increases of ammonium burden in eastern China and
486 northeastern India in MTC_WGT and MTC_SPLC, compared to MTC_SLOW, where the

487 ammonium burden is high in MTC_SLOW (Figure S4).

488 As shown in Figures 2d and 2e, there are large relative differences (>200%) caused
489 by the MTC treatments over the Antarctic and regions between 40ºS and 40ºN where
490 nitrate burden is quite low (<0.6 mg m^{-2} in MTC_SLOW). The increase of nitrate burden
491 over the Antarctic is mainly in the fine mode (Figures 3b and 3c). Compared to
492 MTC_SLOW, the coarse mode nitrate burden in MTC_WGT has a larger relative
493 increase than the fine mode burden (178% versus 91%), which results in a decrease of
494 fine mode fraction from 36.9 to 28.7%. As shown in Figure 3e, fine mode fractions are
495 greatly reduced over oceans and some continental regions between 60ºS and 60ºN. The
496 decrease of coarse mode nitrate burden and the increase of fine mode nitrate burden in
497 MTC_SPLC increase the fine mode fraction from 28.7% in MTC_WGT to 40.9%, which
498 is even higher than that in MTC_SLOW. Considerable increases in the fine mode fraction
499 are found over Eurasia, North America, and the Arctic (Figure 3f). Latitude-altitude cross
500 sections of annually averaged zonal mean nitrate concentrations are shown in Figure S5.

501 Table 4 compares the mass budgets of nitrate in this study with results from previous
502 studies. The mass budgets of our three experiments are within the range (minimum to
503 maximum) of the mass budgets from B17. MTC_SLOW produces lower nitrate burden
504 than the mean value of B17, while both MTC_WGT and MTC_SPLC produce higher
505 nitrate burden than the mean value of B17. All three experiments have shorter lifetime
506 than B17. In B17, large uncertainties are also found in the simulated global tropospheric
507 (pressure > 100 hPa) HNO_3 burdens, ranging from 0.15 to 1.3 Tg N, which contributes to

508 the large spread in simulated nitrate burdens as well. All three experiments produce lower
509 HNO_3 burden than L21 and the mean value of B17 (Table S3). Due to stronger chemical
510 production of nitrate aerosols, MTC_WGT and MTC_SPLC have less HNO_3 burden than
511 MTC_SLOW. In many GCMs that participated in AeroCom phase III experiments, nitrate
512 aerosols are not well represented. They neglect nitrate formation in the coarse mode
513 and/or repeatedly use TEQMs in the coarse mode as in the fine mode. We select 4 GCMs
514 (EMAC, EMEP, GMI, and INCA) which simulate the formation of nitrate aerosols in
515 both fine and coarse mode and consider the heterogeneous reactions on dust and sea salt
516 particles. The selected 4 GCMs give similar mass budgets to those from 9 GCMs (e.g.,
517 nitrate burden of 0.15 Tg N versus 0.14 Tg N) but with a narrow range of values. The fine
518 mode fraction in the four GCMs ranges from ~20% (EMEP) to ~50% (EMAC, GMI, and
519 INCA).

520 The global annual mean nitrate burden in MTC_SLOW is slightly lower than the one
521 from L21, and the net chemistry production in MTC_SLOW is quite close to that in L21
522 (12.8 versus 12.3 Tg N a^{-1}). In MTC_SLOW, MOSAIC is coupled with MAM4 in
523 EAMv2 following L21, which uses quite low α_{HNO_3} in the accumulation, Aitken, and
524 coarse mode. L21 also coupled MOSAIC with MAM7 in CESM2 and found that the
525 nitrate burden increases from 0.11 in MAM4 to 0.135 Tg N in MAM7. The latter is close
526 to the one from Z21 (0.139 Tg N). As we introduced in section 2.3, a high value of 0.65 is
527 used for α_{HNO_3} in the fine sea salt and coarse sea salt modes of MAM7, while equation
528 (5) ($\alpha_{HNO_3} \leq 0.0011$) is applied in the accumulation, Aitken, fine dust, and coarse dust

529 modes. In Z21 and L21, the coupling between MOSAIC and MAM7 partly considers the
530 high α_{HNO_3} on sea salt particles in calculating the mass transfer between HNO_3 and
531 nitrate aerosols, which leads to the increase of net production from gas-aerosol exchange
532 and further results in the increase of nitrate burden. The nitrate burden in MTC_SPLC is
533 slightly higher than that in Z21 and L21 using MAM7. Note that equation (5) is also used
534 in the accumulation modes of MAM7 in Z21 and L21, indicating that there may be
535 underestimation of net accumulation mode chemistry production as well as nitrate
536 burdens in Z21 and L21 using MAM7. Z21 has less dry deposition and longer lifetime of
537 nitrate aerosols than MTC_SLOW, partly because CESM2 reduces the geometric
538 standard deviations in the accumulation and coarse modes from 1.8, used in E3SMv2 and
539 CESM1, to 1.6 and 1.2, respectively (Wu et al., 2020). In EAMv2, the bottom model
540 layer is thinner than the one from CESM1 and CESM2, which can also affect the dry
541 deposition and lifetime of nitrate aerosols (Wu et al., 2020). The two studies (Feng &
542 Penner, 2007; Xu & Penner, 2012) using the HDYN approach produce similar mean
543 nitrate burden, which is larger than that in Z21 and L21.
544

545 **3.3. Surface Concentrations of Nitrate, Ammonium, and Sulfate Aerosols and**
546 **Precursor Gases**

547 Figures 4 and 5 evaluate modeled surface mass concentrations of aerosols (nitrate,
548 ammonium, and sulfate) and precursor gases (HNO_3, NH_3, and SO_2) against
549 ground-based observations from CASTNET and AMoN over U.S., EMEP over Europe,

550 and EANET over East Asia. Mean surface molar concentrations of aerosols and precursor
551 gases are listed in Table S4. In general, all three experiments overestimate nitrate surface
552 concentrations in U.S., Europe, and East Asia (Figures 4a–4c) due to the high model
553 biases of HNO_3 (Figures 5a–5c). Modeled nitrate concentrations in MTC_SLOW agree
554 with the observations reasonably well, especially at EMEP and EANET sites, with
555 smaller biases than those in MTC_WGT and MTC_SPLC. MTC_WGT and MTC_SPLC
556 produce quite similar nitrate concentrations (within 1% differences). They both have a
557 significant increase in the annual mean value (by ~130%), which exacerbates the high
558 biases in MTC_SLOW, whereas the large high biases of HNO_3 in the two experiments
559 are reduced. Compared to MTC_SLOW, the increase of nitrate surface concentrations in
560 MTC_WGT and MTC_SPLC at the three networks corresponds to the increase of nitrate
561 burden over U.S., Europe, and East Asia in Figure 2. MTC_WGT and MTC_SPLC
562 substantially reduce the net loss of fine mode nitrate through gas-aerosol exchange and
563 therefore increase the net chemistry production. Note that the two experiments also have
564 stronger correlation (R) between modeled and observed nitrate surface concentrations.
565 We also found similar high model biases of HNO_3 surface concentrations in Z21 and L21
566 at CASTNET, EMEP, and EANET sites (Figure S6). In B17, most GCMs overestimate
567 HNO_3 surface concentrations with a ratio up to 3.9 over U.S. We further compare
568 modeled surface concentrations of NO_x and NO_2 with ground-based observations and
569 found fairly strong low biases of NO_x at AQS and EANET sites and modest high biases
570 of NO_2 at EMEP (Figure S7). The low biases of NO_x at U.S. and East Asia sites

571 counteract the high biases of HNO_3 and nitrate aerosols (comparing Figure S7 to Table
572 S3), which suggests no strong bias in the NO_x emissions for these regions. For regions
573 where E3SM-MOSAIC has low biases of NO_x but high biases of HNO_3, it might indicate
574 too rapid photochemical conversion of NO_x to HNO_3. Also, the high biases of HNO_3 in
575 these surface comparisons may be caused by slow wet and/or dry deposition, and this
576 could contribute to the high biases of nitrate aerosols. Note that observations of NO_x and
577 NO_2 are not collocated with HNO_3 measurements, especially for AQS.

578 MTC_SLOW slightly underestimates ammonium surface concentrations at
579 CASTNET and EMEP sites (Figures 4d and 4e) but slightly overestimates the
580 concentrations at EANET sites (Figure 4f). The large increase of ammonium surface
581 concentrations in MTC_WGT and MTC_SPLC at the three networks (relative differences
582 around 67%, 107%, and 52%, respectively) indicates that the increase of nitrate surface
583 concentrations in the two experiments is mainly contributed by the increase of NH_4NO_3
584 in the accumulation and Aitken modes. The three experiments underestimate NH_3 surface
585 concentrations at AMoN and EANET sites (Figures 5d and 5f) but overestimate the
586 concentrations at EMEP sites (Figure 5e). The three experiments produce quite close
587 sulfate surface concentrations (~1%) and agree with the observations very well (relative
588 differences around –6%, –17%, and –3%, respectively) (Figures 4g–4i). Modeled SO_2
589 surface concentrations have high biases at CASTNET and EMEP sites (Figures 5g and
590 5h), which is consistent with the performance of CAM-chem in Tilmes et al. (2015) and
591 CAM5 in Liu et al. (2012). The slight underestimation of SO_2 surface concentrations at

592 EANET sites (Figure 5i) is likely attributable to the underestimation of anthropogenic
593 SO_2 emissions in East Asia (e.g., Fan et al., 2018).

594 Figures 6-8 show the seasonal variations of modeled nitrate surface concentrations in
595 comparison with observations at selected CASTNET, EMEP, and EANET sites. We select
596 the CASTNET and EMEP sites following A19. In Figures 6a, 6b and 6d, observed nitrate
597 surface concentrations have their maximum in DJF because of low temperature and
598 sulfate concentrations (Figure S8) and their minimum in JJA due to high temperature and
599 strong precipitation (Pye et al., 2008; Walker et al., 2012), which is typical in eastern and
600 central U.S. All three experiments overestimate the nitrate surface concentrations in all
601 seasons due to high model biases of HNO_3 (Figure S9). MTC_WGT and MTC_SPLC
602 significantly increase the nitrate surface concentrations due to the increase in net fine
603 mode chemistry production, and they have much stronger seasonal contrast than
604 MTC_SLOW and observations at the three sites. The high model biases are larger than 4
605 $\mu g\ m^{-3}$ in DJF, but they can be as low as ~1 $\mu g\ m^{-3}$ in JJA (e.g., Caddo Valley).

606 Unlike Beltsville, Mackville, and Caddo Valley where observed nitrate surface
607 concentrations are close to ammonium concentrations, Everglades NP in Florida has
608 much higher observed nitrate concentrations than ammonium concentrations (Figure S10).
609 The surface molar concentrations of nitrate (~24 nmol m^{-3}) are slightly higher than those
610 of ammonium (~22 nmol m^{-3}). This suggests that the formation of coarse mode $NaNO_3$
611 and $Ca(NO_3)_2$ through heterogeneous reactions with dust and sea salt largely contributes
612 to the nitrate concentrations. Modeled nitrate surface concentrations have small seasonal

613 variations with their maximum in December, while the maximum of observations occurs
614 in March. All three experiments underestimate the nitrate surface concentrations at
615 Joshua Tree NP in California and produce an opposite seasonal cycle. As the three
616 MOSAIC experiments overestimate HNO_3 (Figure S9), underestimate NH_3, and produce
617 ammonium and sulfate concentrations close to observations (Figures S8 and S10), the
618 nitrate formation at Joshua Tree NP may be ammonia-limited (Walker et al. 2012),
619 causing the low biases of modeled nitrate surface concentrations. At Denali NP in Alaska,
620 all three experiments overestimate nitrate surface concentrations in all seasons with their
621 maximum in DJF. Similarly, we find that MTC_WGT and MTC_SPLC produce higher
622 nitrate surface concentrations than MTC_SLOW in all seasons and have stronger
623 seasonal variations than MTC_SLOW at some EMEP and EANET sites. In Figures 7a
624 and 7d-7f, observed nitrate surface concentrations have their maximum in April likely
625 due to the seasonal variations of NH_3 emissions. We also find some improvements of
626 nitrate seasonality in Figures 7d-7f, especially at Malin Head.
627

628 **3.4. Vertical Profiles of Nitrate Aerosols**

629 In this section, we compare modeled vertical profiles of nitrate aerosols with
630 measurements from aircraft campaigns. As shown in Figure 9, flights during INTEX-B,
631 ARCTAS, DC3, and SEAC^{4}RS mainly cover North America where nitrate burden is
632 largely contributed by fine mode nitrate (Figure 3). These field experiments were
633 conducted during our simulation period (2005-2014), mostly in MAM and JJA. In

634 general, MTC_SLOW significantly underestimates PM_4 nitrate concentrations below/at
635 500 hPa, compared to the observations, while MTC_WGT and MTC_SPLC substantially
636 increase the concentrations and improve the model performance below/at 500 hPa
637 (Figure 10). MTC_WGT and MTC_SPLC overestimate PM_4 nitrate concentrations above
638 400 hPa and sometimes exacerbate the high model biases there. All three experiments
639 overestimate HNO_3 concentrations over continental U.S. as well as Alaska (Figure S11),
640 but it is not as significant as the high model biases of HNO_3 surface concentrations at
641 CASTNET sites (Figure 5).

642 In Figure 10a, the high nitrate concentrations below 650 hPa, especially the spike at
643 750 hPa are not captured by model simulations, possibly because we use monthly mean
644 model output to get the profiles while the observed high nitrate concentrations are due to
645 episodic pollution plumes over the Gulf of Mexico (Singh et al., 2009). The observed
646 high nitrate concentrations from ARCTAS flights, such as the spike at 600 hPa in Figure
647 10d, large values below 600 hPa in Figure 10e, and the spike at 700 hPa in Figure 10f,
648 are likely caused by fire plumes from Siberia, California, and Saskatchewan (Jacob et al.,
649 2010). In Figure 10d, MTC_WGT and MTC_SPLC slightly overestimate the nitrate
650 concentrations below 800 hPa in April, while MTC_SLOW has a better agreement with
651 the observations. This is consistent with the comparison of nitrate surface concentrations
652 at Denali NP in April (Figure 6f). In Figure 10e, the large low model biases of nitrate
653 concentrations below 600 hPa, mostly based on measurements over California, are
654 consistent with the comparison of nitrate surface concentrations at Joshua Tree NP in

June (Figure 5e). In Figures 10g-10j, all three experiments underestimate the nitrate concentrations below 500 hPa, which is different from the comparison of nitrate surface concentrations (Figure 4). The large spike at 600 hPa in Figure 10i is mostly caused by wildfires in western U.S. (Toon et al., 2016).

As shown in Figure 11, ATom flights cover vast areas over the Pacific and Atlantic Ocean, where the nitrate concentrations are mainly contributed by particles in the coarse mode, and they were conducted in all seasons. We divide the observations and model results, which are interpolated from monthly mean output along the flight tracks, into 8 sectors. Since the entire ATom campaigns were conducted during 2016-2018, we use the 10-yr averaged monthly model results for the comparison. Similarly, we find that MTC_SLOW underestimates PM_4 nitrate concentrations below/at 500 hPa over the Pacific and Atlantic, while MTC_WGT increases the concentrations and improves the model performance below/at 500 hPa (Figure 12). Nitrate concentrations from MTC_SPLC and MTC_WGT are close except for the regions strongly influenced by outflow of Sahara dust (Figures 12f and 12g), where MTC_WGT produces considerably higher nitrate concentrations (closer to observations) than MTC_SPLC. This is consistent with the higher nitrate burden over dust source regions in MTC_WGT than MTC_SPLC (Figure 2). Modeled HNO_3 concentrations agree well with the observations above 600 hPa (Figure S12). High model biases of HNO_3 concentrations are found over the tropical Atlantic, North Atlantic, North Pacific and Arctic, while low biases occur over the South Atlantic, South Pacific, tropical Pacific, and Antarctic. As shown in Figure 12a, all three

676 experiments overestimate nitrate concentrations below 800 hPa over the Arctic, where
677 there are high model biases of HNO_3. This is consistent with the comparison of nitrate
678 surface concentrations at Denali NP in all seasons.
679

680 **3.5. Radiative Forcing of Nitrate Aerosols**

681 Figure 13 shows RFari and RFaci of nitrate aerosols between PD (2005-2014) and PI
682 (1850) from the three MOSAIC experiments. RFari and RFaci are calculated as the
683 differences of REari and REaci, respectively, between the corresponding PD and PI
684 experiments. In Figures 13a-13c, strong cooling signals are found over East Asia and
685 India, where PD nitrate burden is high. MTC_WGT and MTC_SPLC produce larger
686 RFari (–0.048 and –0.051 W m^{-2}, respectively) than MTC_SLOW (–0.021 W m^{-2})
687 because of the increase in fine mode burden over these regions (Figure 3). The RFari in
688 MTC_SLOW is larger than that from L21 (–0.014 W m^{-2}, see Table 5), because
689 MTC_SLOW has higher PD nitrate burden in the fine mode than L21 (0.036 versus 0.030
690 Tg N). The RFari from the three experiments is within the range (–0.12 to –0.02 W m^{-2})
691 of AeroCom phase II models (Myhre et al., 2013) and near the upper end of the range (–
692 0.3 to –0.03 W m^{-2}) from IPCC AR5 (Boucher et al., 2013). The RFari from MTC_SPLC
693 is close to H14 and B07, but it is still lower than the estimates from A19, B11, and XP12,
694 which mostly depends on the amount of fine mode nitrate. The RFari of ammonium
695 aerosols is –0.068, –0.075, and –0.076 W m^{-2} (Figure S13), respectively.

696 As shown in Figures 13d-13f, there are consistently negative values of RFaci over

North America, North Atlantic, Europe, Central Asia, Siberia, Tibetan Plateau, and North Pacific. Most of the areas pass the significant test (10%), which is different from the noisy spatial pattern of RFaci in Z21. Interestingly, we find similar warming signals over China as in Z21, which results from reduced cloud droplet number concentration differences (with and without nitrate formation) between PD and PI. This may be caused by the competition between the formation of coarse mode nitrate and accumulation mode sulfate for water vapor (Lu et al., 2021). The spatial pattern of the RFaci between 30ºS and 30ºN looks noisy, but the mean values (30ºS-30ºN) are still negative (–0.140, –0.232, and –0.256 W m^{-2}, respectively). MTC_WGT and MTC_SPLC produce much stronger RFaci (–0.332 and –0.352 W m^{-2}, respectively) than MTC_SLOW (–0.244 W m^{-2}), as the increased fine mode nitrate leads to more CCN and cloud droplets in the former experiments.

4. Discussion and Conclusions

In this study, we implement the MOSAIC module (Zaveri et al., 2008) in E3SMv2 to simulate the spatiotemporal distributions of nitrate aerosols and estimate their radiative forcings due to aerosol-radiation and aerosol-cloud interactions (RFari and RFaci). We also modify the calculation of gas-aerosol mass transfer coefficient (MTC) in MOSAIC to consider different accommodation coefficients of HNO_3 onto dust and non-dust particles. The MTC treatments in MTC_WGT and MTC_SPLC use higher α_{HNO_3} (0.65) onto non-dust and partially-dust particles than that in MTC_SLOW (≤0.0011), which

718 substantially enhance the HNO_3 condensation onto fine and coarse interstitial aerosol
719 particles. It leads to a significant increase of global annual mean nitrate burden from
720 0.096 (MTC_SLOW) to 0.237 (MTC_WGT) and 0.185 Tg N (MTC_SPLC), which is
721 mainly due to the increase of coarse mode nitrate burden. The tropospheric HNO_3 burden
722 reduces from 0.425 (MTC_SLOW) to 0.353 (MTC_WGT) and 0.389 Tg N
723 (MTC_SPLC). The modeled nitrate lifecyle in MTC_SLOW is similar to those in Z21
724 and L21 using CESM. The nitrate and HNO_3 burdens from our three experiments are
725 within the range of those from AeroCom phase III models in B17. The large spread in
726 simulated nitrate burdens from previous studies results from not only their methods of
727 gas-aerosol partitioning but also the large uncertainties in HNO_3 burdens. MTC_WGT
728 and MTC_SPLC increase the nitrate burden around the globe with relatively large
729 increases in East Asia, India, Europe, northeastern U.S., and equatorial Africa, largely
730 resulting from the substantial increase of HNO_3 condensation onto fine mode interstitial
731 aerosol particles. MTC_SPLC has lower production of coarse mode nitrate through
732 gas-aerosol exchange and lower nitrate burden than MTC_WGT, especially over dust
733 source regions.

734 We evaluate modeled surface concentrations of nitrate, HNO_3, and other species
735 against ground-based observations from three regional surface networks (i.e., CASTNET
736 over U.S., EMEP over Europe, and EANET over East Asia). Simulated nitrate surface
737 concentrations in MTC_SLOW agree with the observations reasonably well, especially
738 over Europe and East Asia, with small normalized mean biases (NMBs) of 51.5%, 1.4%,

739 and 20.1% respectively. MTC_WGT and MTC_SPLC significantly increase nitrate
740 concentrations, which exacerbates the high biases and gives NMBs of ~260%, ~125%,
741 and ~170%, respectively, for the three networks. All three experiments, particularly
742 MTC_SLOW, significantly overestimate HNO_3 surface concentrations, which also results
743 in too large concentrations of combined nitrate aerosols and HNO_3 gas. Thus, the better
744 agreement of nitrate surface concentrations with observations in MTC_SLOW should be
745 viewed with caution, because MTC_SLOW gives the largest NMBs (176-322%) for
746 HNO_3 at the three networks. These high biases of HNO_3 surface concentrations are also
747 found in Z21, L21, and most GCMs in B17. Seasonal variations of simulated and
748 observed nitrate surface concentrations are compared at selected sites. MTC_WGT and
749 MTC_SPLC produce higher nitrate surface concentrations than MTC_SLOW in all
750 seasons and have stronger seasonal variations than MTC_SLOW at many sites.

751 We compare simulated vertical profiles of PM_4 nitrate concentrations with aircraft
752 measurements from INTEX-B, ARCTAS, DC3, and SEAC^{4}RS field campaigns that were
753 conducted mainly in MAM and JJA over North America. MTC_SLOW significantly
754 underestimates PM_4 nitrate concentrations below 500 hPa compared with the
755 observations, while MTC_WGT and MTC_SPLC substantially increase the nitrate
756 concentrations and improve the model performance below 500 hPa. We also compare
757 simulated vertical profiles of PM_4 nitrate concentrations with measurements from ATom
758 campaigns that were conducted in all seasons over vast areas in the Pacific and Atlantic
759 Ocean. Similarly, we find that MTC_SLOW underestimates PM_4 nitrate concentrations

760 below 400 hPa over the Pacific and Atlantic, while MTC_WGT increases the
761 concentrations and improves the model performance below 400 hPa. MTC_SPLC
762 produces considerably lower nitrate concentrations than MTC_WGT in the tropical and
763 North Atlantic, where nitrate formation processes are strongly influenced by outflow of
764 Sahara dust. Unlike the comparisons of nitrate and HNO_3 surface concentrations with
765 ground-based observations showing high biases, MTC_WGT and MTC_SPLC tend to
766 improve the model performance in simulating vertical profiles of nitrate and HNO_3. We
767 do not find significant overall high biases of HNO_3 concentrations in the troposphere
768 from the five campaigns, especially near the surface. It should be noted that the
769 comparisons with aircraft measurements are subject to considerable spatiotemporal
770 representativeness errors, given the very limited coverage of flight tracks. More
771 measurements of vertical profiles of nitrate and HNO_3 concentrations as well as
772 ground-based observations in the SH, South Asia, and East Asia are needed to evaluate
773 and constrain the model performance.

774 Large RFari values are found over East Asia and India where present-day nitrate
775 burden is high. MTC_WGT and MTC_SPLC produce larger RFari (–0.048 and –0.051 W
776 m^{-2}, respectively) than MTC_SLOW (–0.021 W m^{-2}) because of the increase in fine
777 mode burden. There are consistently negative values of RFaci over North America, North
778 Atlantic, Europe, Central Asia, Siberia, Tibetan Plateau, and North Pacific in all three
779 experiments. The RFari from all three experiments is within the range (–0.12 to –0.02 W
780 m^{-2}) of AeroCom phase II models (Myhre et al., 2013) and near the upper end of the

781 range (–0.3 to –0.03 W m^{-2}) from IPCC AR5 (Boucher et al., 2013). MTC_WGT and
782 MTC_SPLC produce a stronger RFaci (–0.332 and –0.352 W m^{-2}, respectively) than
783 MTC_SLOW (–0.244 W m^{-2}), as the increased fine mode nitrate aerosols lead to more
784 CCN and consequently impact on cloud properties.

785 The sensitivity of simulated nitrate aerosol to the MTC treatments in this study
786 suggests that a model version in which dust and sea salt particles are treated as externally
787 mixed (i.e., in separate modes) from each other and from anthropogenic particles should
788 be developed.

789

790 **Data Availability Statement**

791 CASTNET data can be downloaded from https://www.epa.gov/castnet. AQS data can be
792 downloaded from https://www.epa.gov/outdoor-air-quality-data. AMoN data can be
793 downloaded from http://nadp.slh.wisc.edu/amon/. EMEP data can be downloaded from
794 https://www.emep.int/. EANET data can be downloaded from
795 https://monitoring.eanet.asia/document/public/index. INTEX-B, ARCTAS, DC3, and
796 SEAC^{4}RS data are available at https://www-air.larc.nasa.gov/data.htm. ATom data are
797 available at https://espo.nasa.gov/atom. The E3SMv2 source code is available at
798 https://github.com/E3SM-Project/E3SM.

799

800 **Acknowledgments**

801 This work is supported by the U.S. Department of Energy (DOE), Office of Science,

Office of Biological and Environmental Research, Earth and Environmental System Modeling program as part of the Energy Exascale Earth System Model (E3SM) project. The Pacific Northwest National Laboratory (PNNL) is operated for DOE by Battelle Memorial Institute under contract DE-AC05-76RLO1830. The work at Lawrence Livermore National Laboratory (LLNL) was performed under the auspices of the U.S. DOE by LLNL under Contract DE-AC52-07NA27344.

References

Abbatt, J. P. D., & Waschewsky, G. C. G. (1998). Heterogeneous interactions of HOBr, HNO_3, O_3, and NO_2 with deliquescent NaCl aerosols at room temperature. *The Journal of Physical Chemistry A*, *102*(21), 3719–3725. https://doi.org/10.1021/jp980932d

Adams, P. J., Seinfeld, J. H., Koch, D., Mickley, L., & Jacob, D. (2001). General circulation model assessment of direct radiative forcing by the sulfate-nitrate-ammonium-water inorganic aerosol system. *Journal of Geophysical Research*, *106*(D1), 1097–1111. https://doi.org/10.1029/2000JD900512

An, Q., Zhang, H., Wang, Z., Liu, Y., Xie, B., Liu, Q., et al. (2019). The development of an atmospheric aerosol/chemistry–climate model, BCC_AGCM_CUACE2.0, and simulated effective radiative forcing of nitrate aerosols. *Journal of Advances in Modeling Earth Systems*, *11*(11), 3816–3835. https://doi.org/10.1029/2019MS001622

Barth, M. C., Cantrell, C. A., Brune, W. H., Rutledge, S. A., Crawford, J. H., Huntrieser, H., et al. (2015). The deep convective clouds and chemistry (DC3) field campaign.

Bulletin of the American Meteorological Society, *96*(8), 1281–1309. https://doi.org/10.1175/BAMS-D-13-00290.1

Bassett, M., & Seinfeld, J. H. (1983). Atmospheric equilibrium model of sulfate and nitrate aerosols. *Atmospheric Environment*, *17*(11), 2237–2252. https://doi.org/10.1016/0004-6981(83)90221-4

Bauer, S. E., Koch, D., Unger, N., Metzger, S. M., Shindell, D. T., & Streets, D. G. (2007). Nitrate aerosols today and in 2030: A global simulation including aerosols and tropospheric ozone. *Atmospheric Chemistry and Physics*, *7*(19), 5043–5059. https://doi.org/10.5194/acp-7-5043-2007

Bellouin, N., Rae, J., Jones, A., Johnson, C., Haywood, J., & Boucher, O. (2011). Aerosol forcing in the Climate Model Intercomparison Project (CMIP5) simulations by HadGEM2-ES and the role of ammonium nitrate. *Journal of Geophysical Research*, *116*(D20), D20206. https://doi.org/10.1029/2011JD016074

Bian, H., Chin, M., Hauglustaine, D. A., Schulz, M., Myhre, G., Bauer, S. E., et al. (2017). Investigation of global particulate nitrate from the AeroCom phase III experiment. *Atmospheric Chemistry and Physics*, *17*(21), 12911–12940. https://doi.org/10.5194/acp-17-12911-2017

Boucher, O., Randall, D., Artaxo, P., Bretherton, C., Feingold, G., Forster, P., et al. (2013). Clouds and aerosols. In T. F. Stocker, et al. (Eds.), *Climate change 2013: The physical science basis. Contribution of working group I to the fifth assessment report of the Intergovernmental Panel on Climate Change* (pp. 571–658). Cambridge, UK/New

York, NY: Cambridge University Press

Chen, Y., Cheng, Y., Ma, N., Wei, C., Ran, L., Wolke, R., et al. (2020). Natural sea-salt emissions moderate the climate forcing of anthropogenic nitrate. *Atmospheric Chemistry and Physics*, *20*(2), 771–786. https://doi.org/10.5194/acp-20-771-2020

Cruz, C. N., Dassios, K. G., & Pandis, S. N. (2000). The effect of dioctyl phthalate films on the ammonium nitrate aerossol evaporation rate. *Atmospheric Environment*, *34*(23), 3897–3905. https://doi.org/10.1016/S1352-2310(00)00173-4

Dassios, K. G., & Pandis, S. N. (1999). The mass accommodation coefficient of ammonium nitrate aerosol. *Atmospheric Environment*, *33*(18), 2993–3003. https://doi.org/10.1016/S1352-2310(99)00079-5

Dentener, F. J., Carmichael, G. R., Zhang, Y., Lelieveld, J., & Crutzen, P. J. (1996). Role of mineral aerosol as a reactive surface in the global troposphere. *Journal of Geophysical Research*, *101*(D17), 22869–22889. https://doi.org/10.1029/96JD01818

Emmons, L. K., Schwantes, R. H., Orlando, J. J., Tyndall, G., Kinnison, D., Lamarque, J.-F., et al. (2020). The Chemistry Mechanism in the Community Earth System Model version 2 (CESM2). *Journal of Advances in Modeling Earth Systems*, *12*(4), e2019MS001882. https://doi.org/10.1029/2019MS001882

Emmons, L. K., Walters, S., Hess, P. G., Lamarque, J.-F., Pfister, G. G., Fillmore, D., et al. (2010). Description and evaluation of the Model for Ozone and Related chemical Tracers, version 4 (MOZART-4). *Geoscientific Model Development*, *3*(1), 43–67. https://doi.org/10.5194/gmd-3-43-2010

865 Fairlie, T. D., Jacob, D. J., Dibb, J. E., Alexander, B., Avery, M. A., van Donkelaar, A., &
866 Zhang, L. (2010). Impact of mineral dust on nitrate, sulfate, and ozone in transpacific
867 Asian pollution plumes. *Atmospheric Chemistry and Physics*, *10*(8), 3999–4012.
868 https://doi.org/10.5194/acp-10-3999-2010
869 Fan, T., Liu, X., Ma, P.-L., Zhang, Q., Li, Z., Jiang, Y., et al. (2018). Emission or
870 atmospheric processes? An attempt to attribute the source of large bias of aerosols in
871 eastern China simulated by global climate models. *Atmospheric Chemistry and Physics*,
872 *18*(2), 1395–1417. https://doi.org/10.5194/acp-18-1395-2018
873 Fast, J. D., Gustafson, W. I., Easter, R. C., Zaveri, R. A., Barnard, J. C., Chapman, E. G.,
874 et al. (2006). Evolution of ozone, particulates, and aerosol direct radiative forcing in
875 the vicinity of Houston using a fully coupled meteorology–chemistry–aerosol model.
876 *Journal of Geophysical Research*, *111*(D21), D21305.
877 https://doi.org/10.1029/2005JD006721
878 Feng, Y., & Penner, J. E. (2007). Global modeling of nitrate and ammonium: Interaction
879 of aerosols and tropospheric chemistry. *Journal of Geophysical Research*, *112*, D01304.
880 https://doi.org/10.1029/2005JD006404
881 Fisher, J. A., Jacob, D. J., Travis, K. R., Kim, P. S., Marais, E. A., Chan Miller, C., et al.
882 (2016). Organic nitrate chemistry and its implications for nitrogen budgets in an
883 isoprene- and monoterpene-rich atmosphere: constraints from aircraft (SEAC4RS) and
884 ground-based (SOAS) observations in the Southeast US. *Atmospheric Chemistry and*
885 *Physics*, *16*(9), 5969–5991. https://doi.org/10.5194/acp-16-5969-2016

886 Fountoukis, C., & Nenes, A. (2007). ISORROPIA II: A computationally efficient
887 thermodynamic equilibrium model for K^+–Ca^{2+}–Mg^{2+}–NH_4^+–Na^+–SO_4^{2-}–NO_3^-–Cl^-–
888 H_2O aerosols. *Atmospheric Chemistry and Physics*, *7*(17), 4639–4659.
889 https://doi.org/10.5194/acp-7-4639-2007
890 Fountoukis, C., Nenes, A., Sullivan, A., Weber, R., Van Reken, T., Fischer, M., et al.
891 (2009). Thermodynamic characterization of Mexico City aerosol during MILAGRO
892 2006. *Atmospheric Chemistry and Physics*, *9*(6), 2141–2156.
893 https://doi.org/10.5194/acp-9-2141-2009
894 Fuchs, N. A., & Sutugin, A. G. (1971). High-dispersed aerosols. In G. M. Hidy & J. R.
895 Brock (Eds.), *Topics in Current Aerosol Research (Part 2)* (pp. 1–200). New York, NY:
896 Elsevier.
897 Gao, Y., Zhao, C., Liu, X., Zhang, M., & Leung, L. R. (2014). WRF-Chem simulations of
898 aerosols and anthropogenic aerosol radiative forcing in East Asia. *Atmospheric*
899 *Environment*, *92*, 250–266. https://doi.org/10.1016/j.atmosenv.2014.04.038
900 Gelaro, R., McCarty, W., Suárez, M. J., Todling, R., Molod, A., Takacs, L., et al. (2017).
901 The Modern-Era Retrospective Analysis for Research and Applications, Version 2
902 (MERRA-2). *Journal of Climate*, *30*(14), 5419–5454.
903 https://doi.org/10.1175/JCLI-D-16-0758.1
904 Gettelman, A., & Morrison, H. (2015). Advanced two-moment bulk microphysics for
905 global models. Part I: Off-line tests and comparison with other schemes. *Journal of*
906 *Climate*, *28*(3), 1268–1287. https://doi.org/10.1175/JCLI-D-14-00102.1

907 Ghan, S. J. (2013). Technical note: Estimating aerosol effects on cloud radiative forcing.
908 *Atmospheric Chemistry and Physics*, *13*(19), 9971–9974.
909 https://doi.org/10.5194/acp-13-9971-2013
910 Golaz, J.-C., Larson, V. E., & Cotton, W. R. (2002). A pdf-based model for boundary
911 layer clouds. Part I: Method and model description. *Journal of the Atmospheric*
912 *Sciences*, *59*(24), 3540–3551.
913 https://doi.org/10.1175/1520-0469(2002)059<3540:APBMFB>2.0.CO;2
914 Golaz, J.-C., Van Roekel, L. P., Zheng, X., Roberts, A. F., Wolfe, J. D., Lin, W., et al.
915 (2022). The DOE E3SM model version 2: Overview of the physical model. Submitted
916 to Journal of Advances in Modeling Earth Systems.
917 Guenther, A. B., Jiang, X., Heald, C. L., Sakulyanontvittaya, T., Duhl, T., Emmons, L. K.,
918 & Wang, X. (2012). The Model of Emissions of Gases and Aerosols from Nature
919 version 2.1 (MEGAN2.1): An extended and updated framework for modeling biogenic
920 emissions. *Geoscientific Model Development*, *5*(6), 1471–1492.
921 https://doi.org/10.5194/gmd-5-1471-2012
922 Guimbaud, C., Arens, F., Gutzwiller, L., Gäggeler, H. W., & Ammann, M. (2002). Uptake
923 of HNO_3 to deliquescent sea-salt particles: a study using the short-lived radioactive
924 isotope tracer ^{13}N. *Atmospheric Chemistry and Physics*, *2*(4), 249–257.
925 https://doi.org/10.5194/acp-2-249-2002
926 Guo, H., Campuzano-Jost, P., Nault, B. A., Day, D. A., Schroder, J. C., Kim, D., et al.
927 (2021). The importance of size ranges in aerosol instrument intercomparisons: a case

928 study for the Atmospheric Tomography Mission. *Atmospheric Measurement*
929 *Techniques*, *14*(5), 3631–3655. https://doi.org/10.5194/amt-14-3631-2021
930 Hao, L. Q., Kortelainen, A., Romakkaniemi, S., Portin, H., Jaatinen, A., Leskinen, A., et
931 al. Atmospheric submicron aerosol composition and particulate organic nitrate
932 formation in a boreal forestland–urban mixed region. *Atmospheric Chemistry and*
933 *Physics*, *14*(24), 13483–13495. https://doi.org/10.5194/acp-14-13483-2014
934 Hauglustaine, D. A., Balkanski, Y., & Schulz, M. (2014). A global model simulation of
935 present and future nitrate aerosols and their direct radiative forcing of climate.
936 *Atmospheric Chemistry and Physics*, *14*(20), 11031–11063.
937 https://doi.org/10.5194/acp-14-11031-2014
938 Hoesly, R. M., Smith, S. J., Feng, L., Klimont, Z., Janssens-Maenhout, G., Pitkanen, T.,
939 et al. (2018). Historical (1750–2014) anthropogenic emissions of reactive gases and
940 aerosols from the Community Emissions Data System (CEDS). *Geoscientific Model*
941 *Development*, *11*(1), 369–408. https://doi.org/10.5194/gmd-11-369-2018
942 Itahashi, S., Hayami, H., Uno, I., Pan, X., & Uematsu, M. (2016). Importance of
943 coarse-mode nitrate produced via sea salt as atmospheric input to East Asian oceans.
944 *Geophysical Research Letters*, *43*(10), 5483–5491.
945 https://doi.org/10.1002/2016GL068722
946 Jacob, D. J., Crawford, J. H., Maring, H., Clarke, A. D., Dibb, J. E., Emmons, L. K., et al.
947 (2010). The Arctic Research of the Composition of the Troposphere from Aircraft and
948 Satellites (ARCTAS) mission: Design, execution, and first results. *Atmospheric*

949 *Chemistry and Physics*, *10*(11), 5191–5212. https://doi.org/10.5194/acp-10-5191-2010
950 Kiendler-Scharr, A., Mensah, A. A., Friese, E., Topping, D., Nemitz, E., Prevot, A. S. H.,
951 et al. (2016). Organic nitrates from night-time chemistry are ubiquitous in the
952 European submicron aerosol. *Geophysical Research Letters*, *43*(14), 7735–7744.
953 https://doi.org/10.1002/2016GL069239
954 Kok, J. F. (2011). A scaling theory for the size distribution of emitted dust aerosols
955 suggests climate models underestimate the size of the global dust cycle. *Proceedings of*
956 *the National Academy of Sciences of the United States of America*, *108*(3), 1016–1021.
957 https://doi.org/10.1073/pnas.1014798108
958 Kulmala, M., Laaksonen, A., Korhonen, P., Vesala, T., Ahonen, T., & Barrett, J. C. (1993).
959 The effects of atmospheric nitric-acid vapor on cloud condensation nucleus activation.
960 *Journal of Geophysical Research*, *98*(D12), 22949–22958.
961 https://doi.org/10.1029/93JD02070
962 Li, J., Wang, Z., Zhuang, G., Luo, G., Sun, Y., & Wang, Q. (2012). Mixing of Asian
963 mineral dust with anthropogenic pollutants over East Asia: a model case study of a
964 super-duststorm in March 2010. *Atmospheric Chemistry and Physics*, *12*(16), 7591–
965 7607. https://doi.org/10.5194/acp-12-7591-2012
966 Liao, H., Adams, P. J., Chung, S. H., Seinfeld, J. H., Mickley, L. J., & Jacob, D. J. (2003).
967 Interactions between tropospheric chemistry and aerosols in a unified general
968 circulation model. *Journal of Geophysical Research*, *108*(D1), 4001.
969 https://doi.org/10.1029/2001JD001260

970 Liao, H., & Seinfeld, J. H. (2005). Global impacts of gas-phase chemistry–aerosol
971 interactions on direct radiative forcing by anthropogenic aerosols and ozone. *Journal*
972 *of Geophysical Research*, *110*(D18), D18208. https://doi.org/10.1029/2005JD005907
973 Liu, X., Easter, R. C., Ghan, S. J., Zaveri, R., Rasch, P., Shi, X., et al. (2012). Toward a
974 minimal representation of aerosols in climate models: Description and evaluation in
975 the Community Atmosphere Model CAM5. *Geoscientific Model Development*, *5*(3),
976 709–739. https://doi.org/10.5194/gmd-5-709-2012
977 Liu, X., Ma, P.-L., Wang, H., Tilmes, S., Singh, B., Easter, R. C., et al. (2016).
978 Description and evaluation of a new four-mode version of the Modal Aerosol Module
979 (MAM4) within version 5.3 of the Community Atmosphere Model. *Geoscientific*
980 *Model Development*, *9*(2), 505–522. https://doi.org/10.5194/gmd-9-505-2016
981 Lu, Z., Liu, X., Zaveri, R. A., Easter, R. C., Tilmes, S., Emmons, L. K., et al. (2021).
982 Radiative forcing of nitrate aerosols from 1975 to 2010 as simulated by MOSAIC
983 module in CESM2-MAM4. *Journal of Geophysical Research: Atmospheres*, *126*(17),
984 e2021JD034809. https://doi.org/10.1029/2021JD034809
985 Ma, P.-L., Harrop, B. E., Larson, V. E., Neale, R. B., Gettelman, A., Morrison, H., et al.
986 (2022). Better calibration of cloud parameterizations and subgrid effects increases the
987 fidelity of E3SM Atmosphere Model version 1. *Geoscientific Model Development*,
988 *15*(7), 2881–2916. https://doi.org/10.5194/gmd-15-2881-2022
989 McNaughton, C. S., Clarke, A. D., Howell, S. G., Pinkerton, M., Anderson, B., Thornhill,
990 L., et al. (2007). Results from the DC-8 Inlet Characterization Experiment (DICE):

991 Airborne versus surface sampling of mineral dust and sea salt aerosols. *Aerosol*
992 *Science and Technology*, *41*(2), 136–159. https://doi.org/10.1080/02786820601118406
993 Metzger, S., Dentener, F., Krol, M., Jeuken, A., & Lelieveld, J. (2002). Gas/aerosol
994 partitioning 2. Global modeling results. *Journal of Geophysical Research*, *107*(D16),
995 4313. https://doi.org/10.1029/2001JD001103
996 Metzger, S., & Lelieveld, J. (2007). Reformulating atmospheric aerosol thermodynamics
997 and hygroscopic growth into fog, haze and clouds. *Atmospheric Chemistry and Physics*,
998 *7*(12), 3163–3193. https://doi.org/10.5194/acp-7-3163-2007
999 Myhre, G., Samset, B. H., Schulz, M., Balkanski, Y., Bauer, S., Berntsen, T. K., et al.
1000 (2013). Radiative forcing of the direct aerosol effect from AeroCom Phase II
1001 simulations. *Atmospheric Chemistry and Physics*, *13*(4), 1853–1877.
1002 https://doi.org/10.5194/acp-13-1853-2013
1003 Naik, V., Szopa, S., Adhikary, B., Artaxo, P., Berntsen, T., Collins, W. D., et al. (2021).
1004 Short-lived climate forcers. In V. Masson-Delmotte, et al. (Eds.), *Climate change 2021:*
1005 *The physical science basis. Contribution of working group I to the sixth assessment*
1006 *report of the Intergovernmental Panel on Climate Change*. Cambridge, UK/New York,
1007 NY: Cambridge University Press. In Press
1008 Nenes, A., Pandis, S. N., & Pilinis, C. (1998). ISORROPIA: A new thermodynamic
1009 equilibrium model for multiphase multicomponent inorganic aerosols. *Aquatic*
1010 *Geochemistry*, *4*(1), 123–152. https://doi.org/10.1023/A:1009604003981
1011 Ng, N. L., Brown, S. S., Archibald, A. T., Atlas, E., Cohen, R. C., Crowley, J. N., et al.

(2017). Nitrate radicals and biogenic volatile organic compounds: oxidation, mechanisms, and organic aerosol. *Atmospheric Chemistry and Physics*, *17*(3), 2103–2162. https://doi.org/10.5194/acp-17-2103-2017

Petters, M., & Kreidenweis, S. (2007). A single parameter representation of hygroscopic growth and cloud condensation nucleus activity. *Atmospheric Chemistry and Physics*, *7*(8), 1961–1971. https://doi.org/10.5194/acp-7-1961-2007

Pye, H. O. T., Chan, A. W. H., Barkley, M. P., and Seinfeld, J. H. (2010). Global modeling of organic aerosol: the importance of reactive nitrogen (NO_x and NO_3). *Atmospheric Chemistry and Physics*, *10*(22), 11261–11276. https://doi.org/10.5194/acp-10-11261-2010

Pye, H. O. T., Liao, H., Wu, S., Mickley, L. J., Jacob, D. J., Henze, D. K., & Seinfeld, J. H. (2009). Effect of changes in climate and emissions on future sulfate–nitrate–ammonium aerosol levels in the United States. *Journal of Geophysical Research*, *114*, D01205. https://doi.org/10.1029/2008JD010701

Pye, H. O. T., Luecken, D. J., Xu, L., Boyd, C. M., Ng, N. L., Baker, K. R. et al. (2015). Modeling the current and future roles of particulate organic nitrates in the Southeastern United States. *Environmental Science & Technology*, *49*(24), 14195–14203. https://doi.org/10.1021/acs.est.5b03738

Rasch, P. J., Xie, S., Ma, P.-L., Lin, W., Wang, H., Tang, Q., et al. (2019). An overview of the atmospheric component of the Energy Exascale Earth System Model. Journal of Earth System Model. *Journal of Advances in Modeling Earth Systems*, *11*(8), 2377–

2411. https://doi.org/10.1029/2019MS001629

Riemer, N., Vogel, H., Vogel, B., Schell, B., Ackermann, I., Kessler, C., & Hass, H. (2003). Impact of the heterogeneous hydrolysis of N_2O_5 on chemistry and nitrate aerosol formation in the lower troposphere under photosmog conditions. *Journal of Geophysical Research*, *108*(D4), 4144. https://doi.org/10.1029/2002JD002436

Rollins, A. W., Browne, E. C., Min, K.-E., Pusede, S. E., Wooldridge, P. J., Gentner, D. R., et al. (2012). Evidence for NOx control over nighttime SOA formation. *Science*, *337*(6099), 1210–1212. https://doi.org/10.1126/science.1221520

Singh, H. B., Brune, W. H., Crawford, J. H., Flocke, F., & Jacob, D. J. (2009). Chemistry and transport of pollution over the Gulf of Mexico and the Pacific: spring 2006 INTEX-B campaign overview and first results. *Atmospheric Chemistry and Physics*, *9*(7), 2301–2318. https://doi.org/10.5194/acp-9-2301-2009

Skeie, R. B., Berntsen, T. K., Myhre, G., Tanaka, K., Kvalevåg, M. M., & Hoyle, C. R. (2011). Anthropogenic radiative forcing time series from pre-industrial times until 2010. *Atmospheric Chemistry and Physics*, *11*(22), 11827–11857. https://doi.org/10.5194/acp-11-11827-2011

Song, C. H., Kim, C. M., Lee, Y. J., Carmichael, G. R., Lee, B. K., & Lee, D. S. (2007). An evaluation of reaction probabilities of sulfate and nitrate precursors onto East Asia dust particles. *Journal of Geophysical Research*, *112*(D18), D18206. https://doi.org/2006JD008092

Tang, Q., Prather, M. J., Hsu, J., Ruiz, D. J., Cameron-Smith, P. J., Xie, S., & Golaz, J.-C.

(2021). Evaluation of the interactive stratospheric ozone (O3v2) module in the E3SM version 1 Earth system model. *Geoscientific Model Development*, *14*(3), 1219–1236. https://doi.org/10.5194/gmd-14-1219-2021

Thompson, C. R., Wofsy, S. C., Prather, M. J., Newman, P. A., Hanisco, T. F., Ryerson, T. B. et al. (2021). THE NASA ATMOSPHERIC TOMOGRAPHY (ATom) MISSION: Imaging the chemistry of the global atmosphere. *Bulletin of the American Meteorological Society*, *96*(8), 1–53. https://doi.org/10.1175/BAMS-D-20-0315.1

Tilmes, S., Lamarque, J.-F., Emmons, L. K., Kinnison, D. E., Ma, P.-L., Liu, X., et al. (2015). Description and evaluation of tropospheric chemistry and aerosols in the Community Earth System Model (CESM1.2). *Geoscientific Model Development*, *8*(5), 1395–1426. https://doi.org/10.5194/gmd-8-1395-2015

Toon, O. B., Maring, H., Dibb, J., Ferrare, R., Jacob, D. J., Jensen, E. J., et al. (2016). Planning, implementation, and scientific goals of the Studies of Emissions and Atmospheric Composition, Clouds and Climate Coupling by Regional Surveys (SEAC^{4}RS) field mission. *Journal of Geophysical Research: Atmospheres*, *121*(9), 4967–5009. https://doi.org/10.1002/2015JD024297

van Dorland, R., Dentener, F. J., & Lelieveld, J. (1997). Radiative forcing due to tropospheric ozone and sulfate aerosols. *Journal of Geophysical Research*, *102*(D23), 28079–28100. https://doi.org/10.1029/97JD02499

van Marle, M., Kloster, S., Magi, B., Marlon, J., Daniau, A., Field, R., et al. (2017). Historic global biomass burning emissions for CMIP6 (BB4CMIP) based on merging

satellite observations with proxies and fire models (1750-2015). *Geoscientific Model Development*, *10*(9), 3329–3357. https://doi.org/10.5194/gmd-10-3329-2017

Walker, J. M., Philip, S., Martin, R. V., & Seinfeld, J. H. (2012). Simulation of nitrate, sulfate, and ammonium aerosols over the United States. *Atmospheric Chemistry and Physics*, *12*(22), 11213–11227. https://doi.org/10.5194/acp-12-11213-2012

Wang, H., Easter, R. C., Zhang, R., Ma, P.-L., Singh, B., Zhang, K., et al. (2020). Aerosols in the E3SM Version 1: New developments and their impacts on radiative forcing. *Journal of Advances in Modeling Earth Systems*, *12*, e2019MS001851. https://doi.org/10.1029/2019MS001851

Wang, Y.-C., Pan, H.-L., & Hsu, H.-H. (2015). Impacts of the triggering function of cumulus parameterization on warm-season diurnal rainfall cycles at the Atmospheric Radiation Measurement Southern Great Plains site. *Journal of Geophysical Research: Atmospheres*, *120*(20), 10681–10702. https://doi.org/10.1002/2015JD023337

Wu, M., Liu, X., Yu, H., Wang, H., Shi, Y., Yang, K., et al. (2020). Understanding processes that control dust spatial distributions with global climate models and satellite observations. *Atmospheric Chemistry and Physics*, *20*(22), 13835–13855. https://doi.org/10.5194/acp-20-13835-2020

Xie, S., Lin, W., Rasch, P. J., Ma, P.-L., Neale, R., Larson, V. E., et al. (2018). Understanding cloud and convective characteristics in version 1 of the E3SM atmosphere model. *Journal of Advances in Modeling Earth Systems*, *10*(10), 2618–2644. https://doi.org/10.1029/2018MS001350

1096 Xie, S., Wang, Y.-C., Lin, W., Ma, H.-Y., Tang, Q., Tang, S., et al. (2019). Improved
1097 diurnal cycle of precipitation in E3SM with a revised convective triggering function.
1098 *Journal of Advances in Modeling Earth Systems*, *11*(7), 2290–2310.
1099 https://doi.org/10.1029/2019MS001702
1100 Xie, S., & Zhang, M. (2000). Impact of the convection triggering function on
1101 single-column model simulations. *Journal of Geophysical Research*, *105*(D11),
1102 14983–14996. https://doi.org/10.1029/2000JD900170
1103 Xu, L., & Penner, J. E. (2012). Global simulations of nitrate and ammonium aerosols and
1104 their radiative effects. *Atmospheric Chemistry and Physics*, *12*(20), 9479–9504.
1105 https://doi.org/10.5194/acp-12-9479-2012
1106 Zaveri, R. A., Berkowitz, C. M., Brechtel, F. J., Gilles, M. K., Hubbe, J. M., et al. (2010).
1107 Nighttime chemical evolution of aerosol and trace gases in a power plant plume:
1108 Implications for secondary organic nitrate and organosulfate aerosol formation, NO_3
1109 radical chemistry, and N_2O_5 heterogeneous hydrolysis. *Journal of Geophysical*
1110 *Research*, *115*(D12), D12304. httsp://doi.org/10.1029/2009JD013250
1111 Zaveri, R. A., Easter, R. C., Fast, J. D., & Peters, L. K. (2008). Model for Simulating
1112 Aerosol Interactions and Chemistry (MOSAIC). *Journal of Geophysical Research*, *113*,
1113 D13204. https://doi.org/10.1029/2007JD008782
1114 Zaveri, R. A., Easter, R. C., Singh, B., Wang, H., Lu, Z., Tilmes, S., et al. (2021).
1115 Development and evaluation of chemistry-aerosol-climate model
1116 CAM5-chem-MAM7-MOSAIC: Global atmospheric distribution and radiative effects

of nitrate aerosol. *Journal of Advances in Modeling Earth Systems*, *13*, e2020MS002346. https://doi.org/10.1029/2020MS002346

Zaveri, R. A., Shilling, J. E., Fast, J. D., & Springston, S. R. (2020). Efficient nighttime biogenic SOA formation in a polluted residual layer. *Journal of Geophysical Research: Atmospheres*, *125*(6), e2019JD031583. https://doi.org/10.1029/2019JD031583.

Zhang, G. J., & McFarlane, N. A. (1995). Sensitivity of climate simulations to the parameterization of cumulus convection in the Canadian climate centre general circulation model. *Atmosphere-Ocean*, *33*(3), 407–446. https://doi.org/10.1080/07055900.1995.9649539

Zhang, Y., Chen, Y., Sarwar, G., & Schere, K. (2012). Impact of gas-phase mechanisms on Weather Research Forecasting Model with Chemistry (WRF/Chem) predictions: Mechanism implementation and comparative evaluation. *Journal of Geophysical Research*, *117*(D1), D01301. https://doi.org/10.1029/2011JD015775

Zhou, C.-H., Gong, S., Zhang, X.-Y., Liu, H.-L., Xue, M., Cao, G.-L., et al. (2012). Towards the improvements of simulating the chemical and optical properties of Chinese aerosols using an online coupled model—CUACE/Aero. *Tellus B: Chemical and Physical Meteorology*, *64*(1), 18965. https://doi.org/10.3402/tellusb.v64i0.18965

Ziemke, J. R., Chandra, S., Duncan, B. N., Froidevaux, L., Bhartia, P. K., Levelt, P. F., & Waters, J. W. (2006). Tropospheric ozone determined from Aura OMI and MLS: Evaluation of measurements and comparison with the Global Modeling Initiative's Chemical Transport Model. *Journal of Geophysical Research*, *111*(D19), D19303.

https://doi.org/10.1029/2006JD007089

Figures

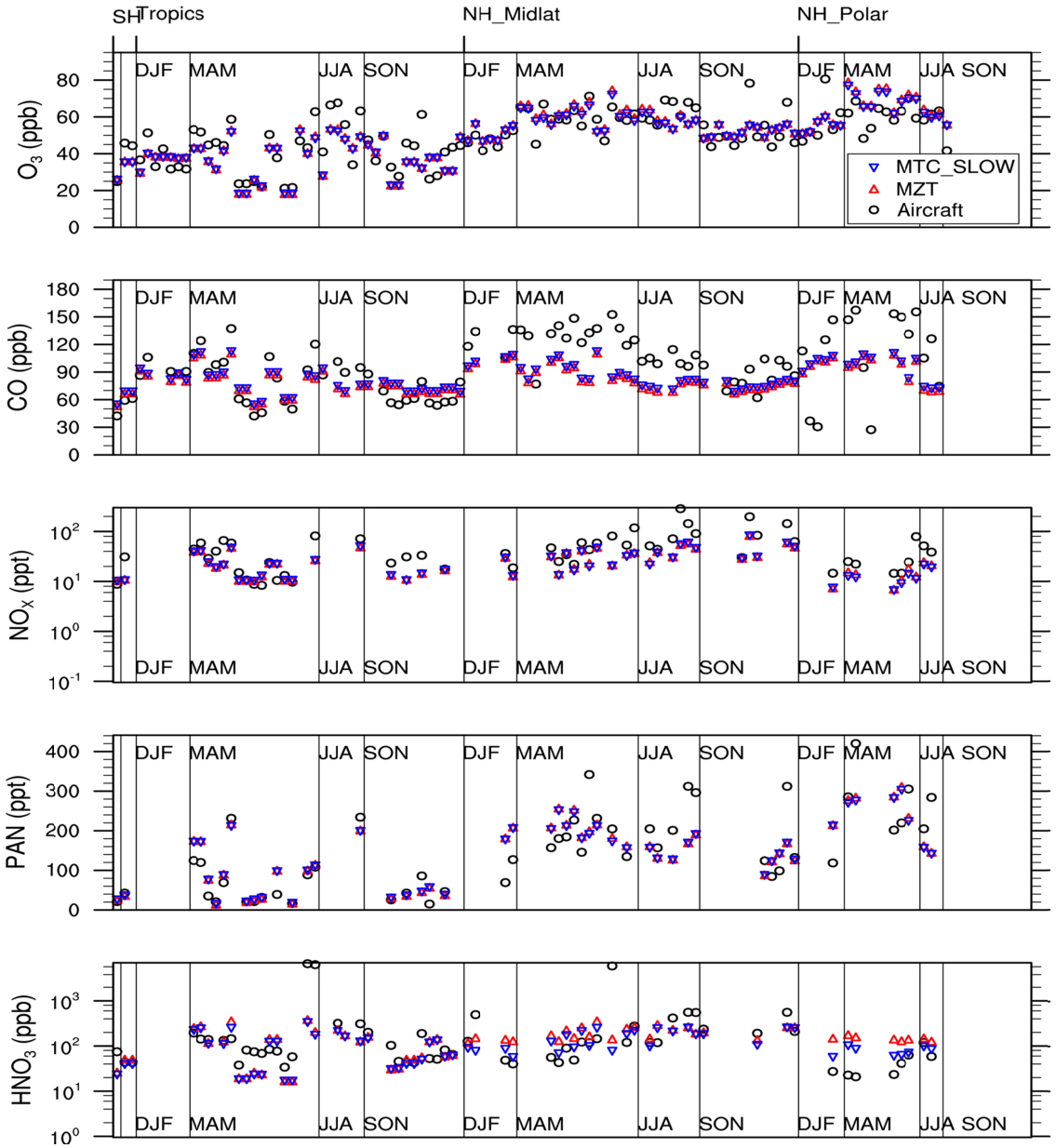

Figure 1. Evaluation of modeled tropospheric O_3, CO, NO_x, PAN, and HNO_3 (averaged over 2005-2014) against observations from aircraft campaigns (operated during 1995-2010), averaged over 2-7 km.

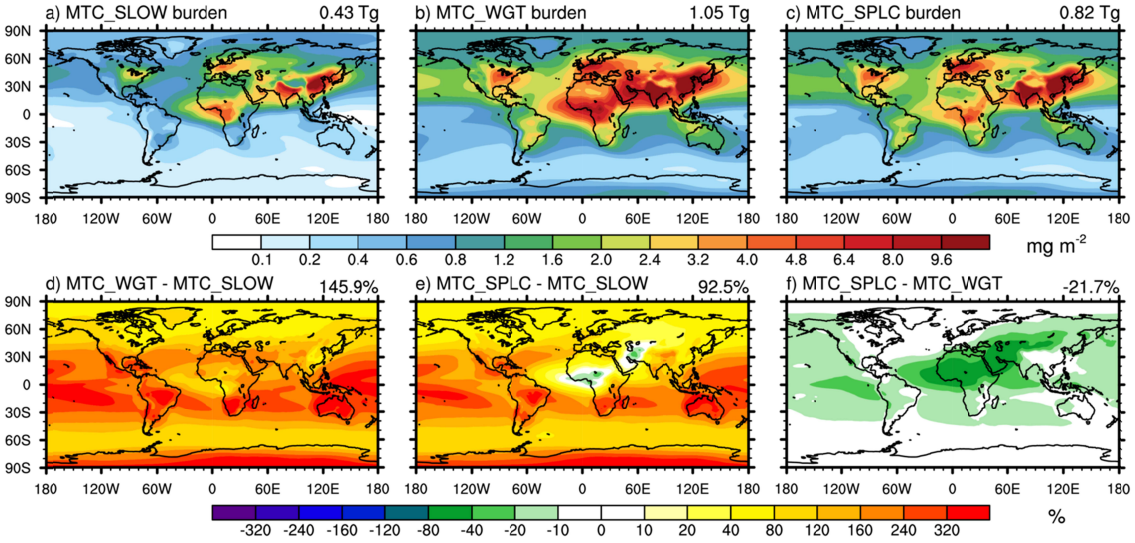

Figure 2. Spatial distributions of global annual mean (a-c) nitrate burden, (d-e) relative differences of nitrate burden compared to MTC_SLOW, and (f) relative differences of nitrate burden (MTC_SPLC) compared to MTC_WGT. Numbers at the top-right of each panel are global annual mean values.

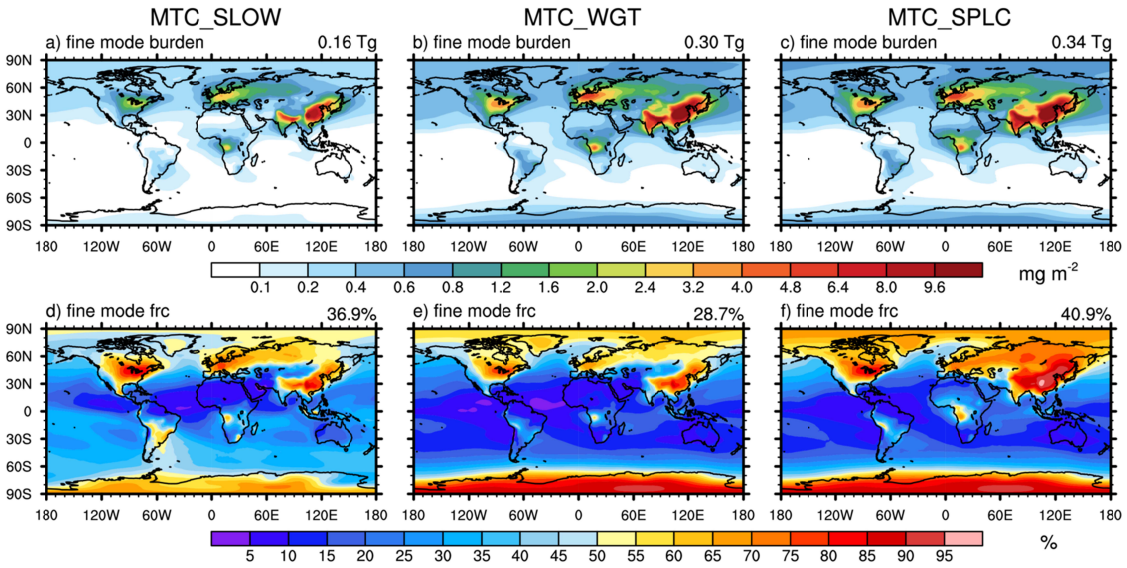

Figure 3. Spatial distributions of global annual mean (a-c) nitrate burden in the fine mode (accumulation and Aitken modes), and (d-f) mass fractions of the fine mode nitrate burden. Numbers at the top-right of each panel are global annual mean values.

1176

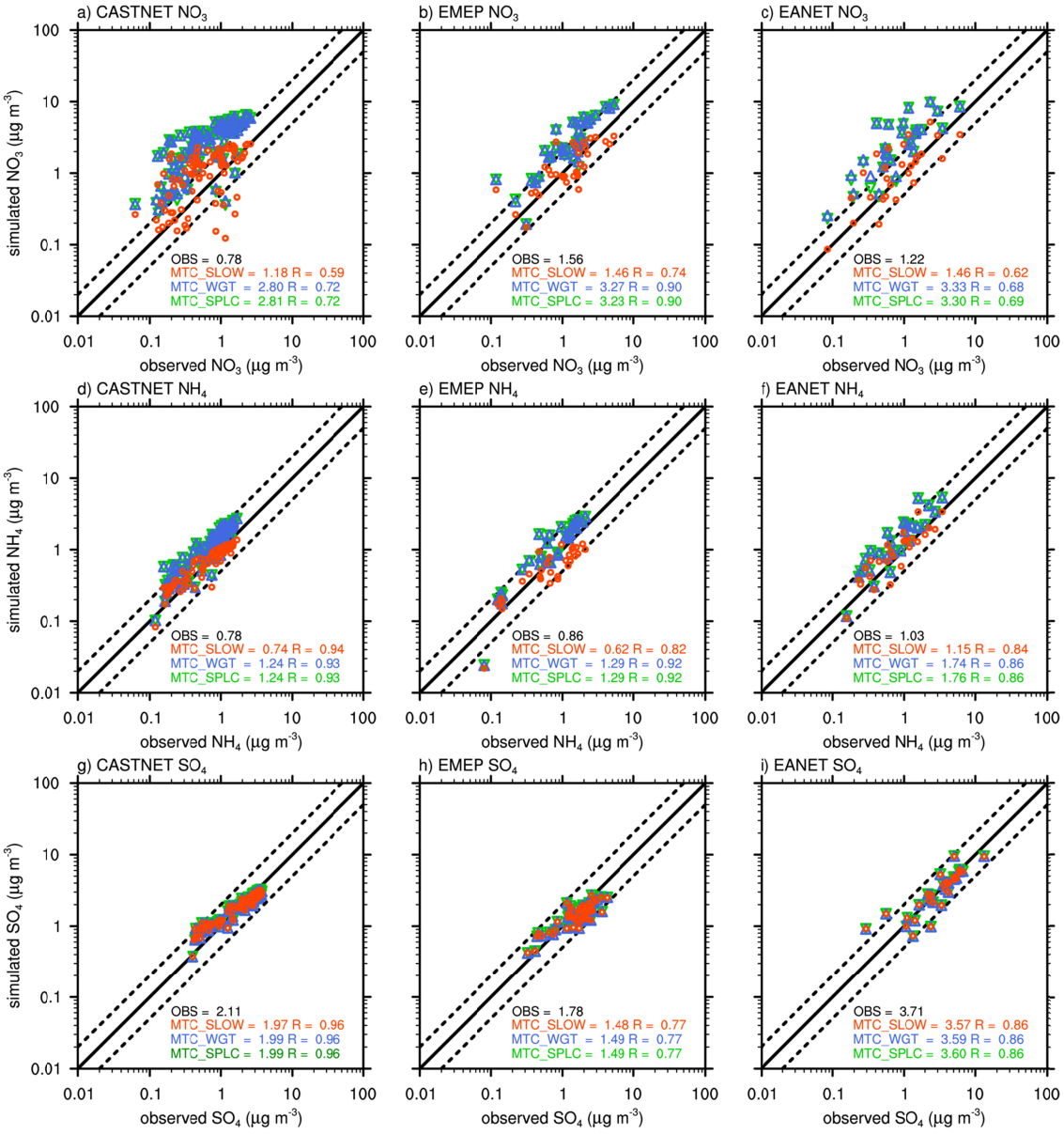

1177

1182 **Figure 4.** Scatter plots of modeled annual mean surface concentrations (μg m^{-3}) of nitrate
1183 (top row), ammonium (middle row), and sulfate (bottom row) aerosols compared to
1184 observations at CASTNET (left column), EMEP (middle column), and EANET (right
1185 column) network sites during 2005-2014. The numbers are mean concentrations and
1186 correlation coefficients.

1183

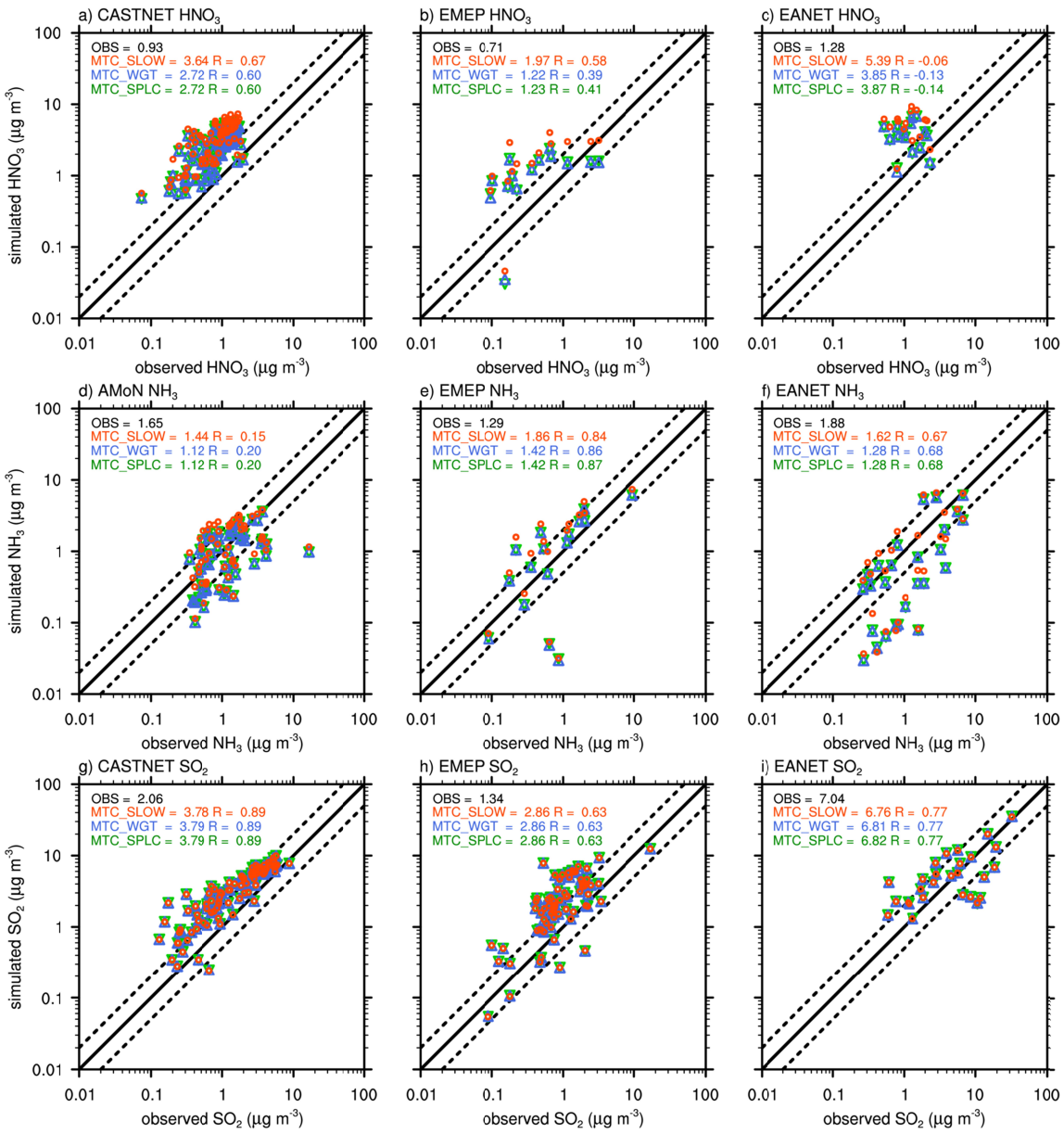

1184

1189 **Figure 5.** Scatter plots of modeled annual mean surface concentrations (μg m^{-3}) of HNO_3

1190 (top row), NH_3 (middle row), and SO_2 (bottom row) compared to observations at

1191 CASTNET and AMoN (left column), EMEP (middle column), and EANET (right column)

1192 network sites during 2005-2014. The numbers are mean concentrations and correlation

1193 coefficients.

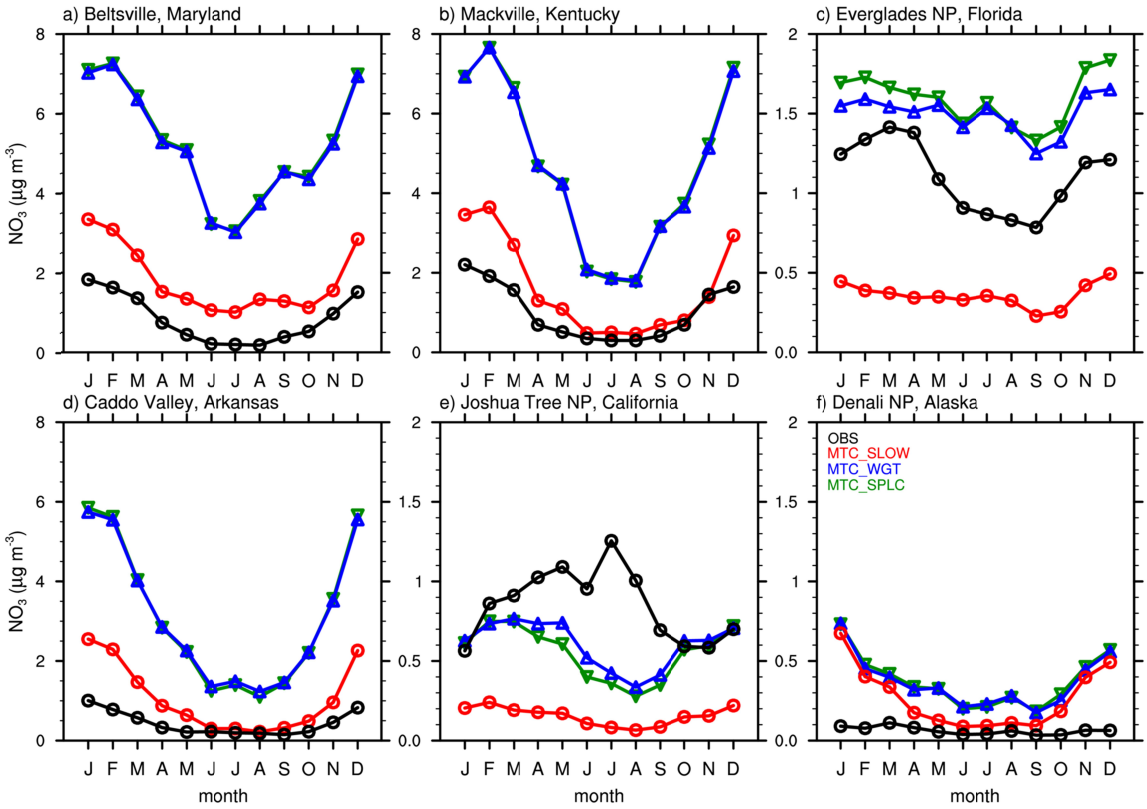

Figure 6. Seasonal variations of simulated (color lines and symbols) and observed (black lines and circles) nitrate surface concentrations (µg m^{-3}) at 6 CASTNET sites: Beltsville (39.0ºN, 76.8ºW), Mackville (37.7ºN, 85.0ºW), Everglades NP (25.4ºN, 80.7ºW), Caddo Valley (34.2ºN, 93.1ºW), Joshua Tree NP (34.1ºN, 116.4ºW), and Denali NP (63.7ºN, 149.0ºW).

1202

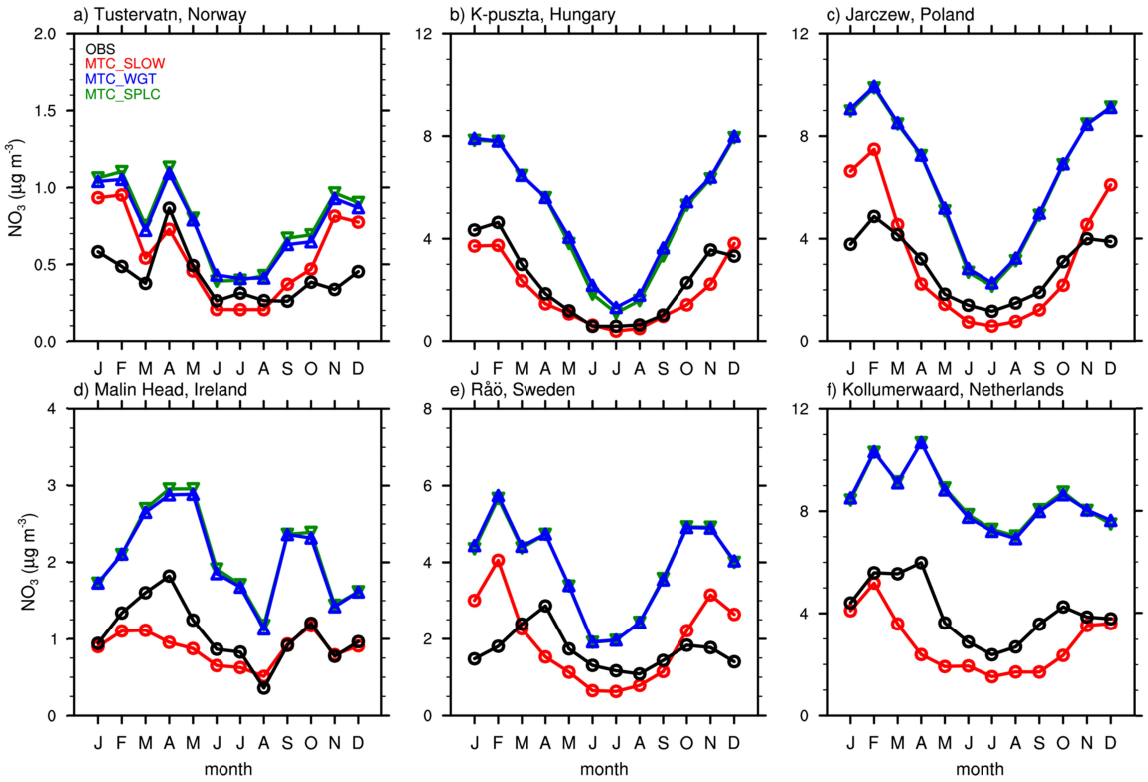

1203

1207 **Figure 7.** Seasonal variations of simulated (color lines and symbols) and observed (black

1208 lines and circles) nitrate surface concentrations (µg m^{-3}) at 6 EMEP sites: Tustervatn

1209 (65.8ºN, 13.9ºE), K-puszta (47.0ºN, 19.6ºE), Jarczew (51.8ºN, 22.0ºE), Malin Head

1210 (55.4ºN, 7.3ºW), Råö (57.4ºN, 11.9ºE), and Kollumerwaard (53.3ºN, 6.3ºE).

1208

1209

1210

1211

1212

1213

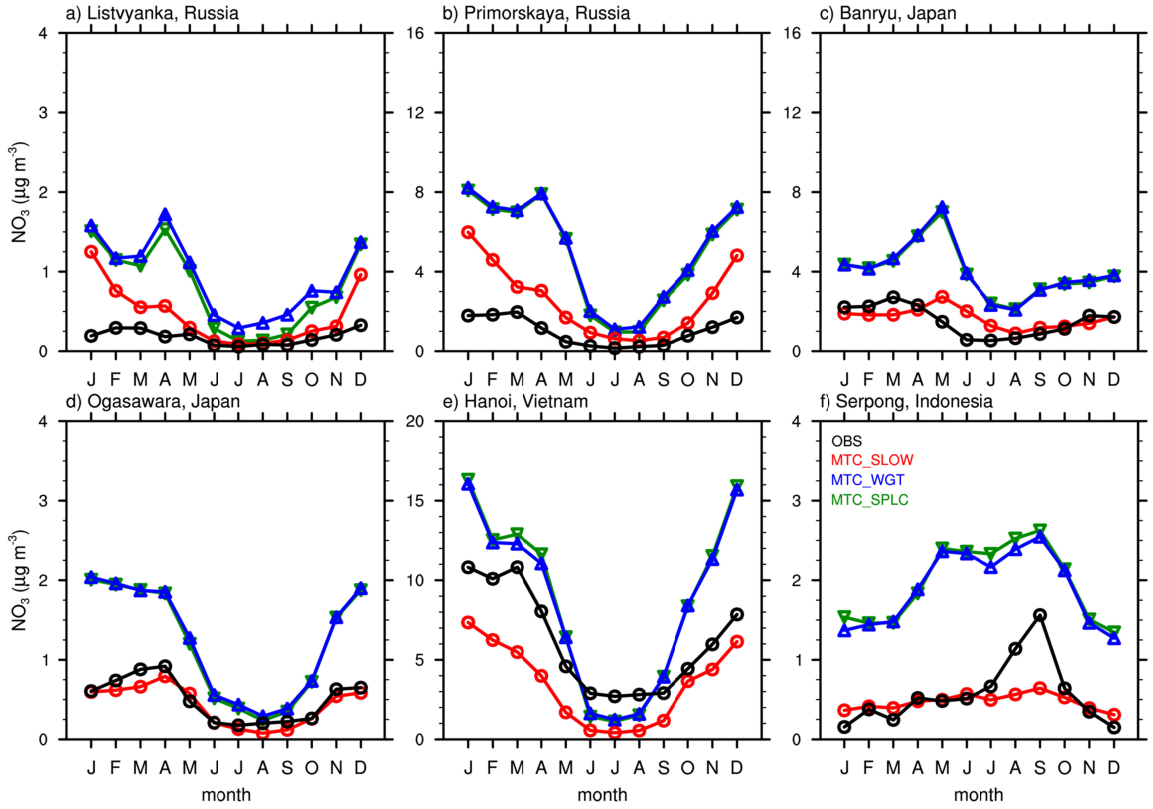

Figure 8. Seasonal variations of simulated (color lines and dots) and observed (black lines and dots) nitrate surface concentrations (μg m^{-3}) at 6 EANET sites: Listvyanka (51.8ºN, 104.9ºE), Primorskaya (43.6ºN, 132.2ºE), Banryu (34.7ºN, 131.8ºE), Ogasawara (27.1ºN, 142.2ºE), Hanoi (21.1ºN, 105.7ºE), and Serpong (6.4ºS, 109.7ºE).

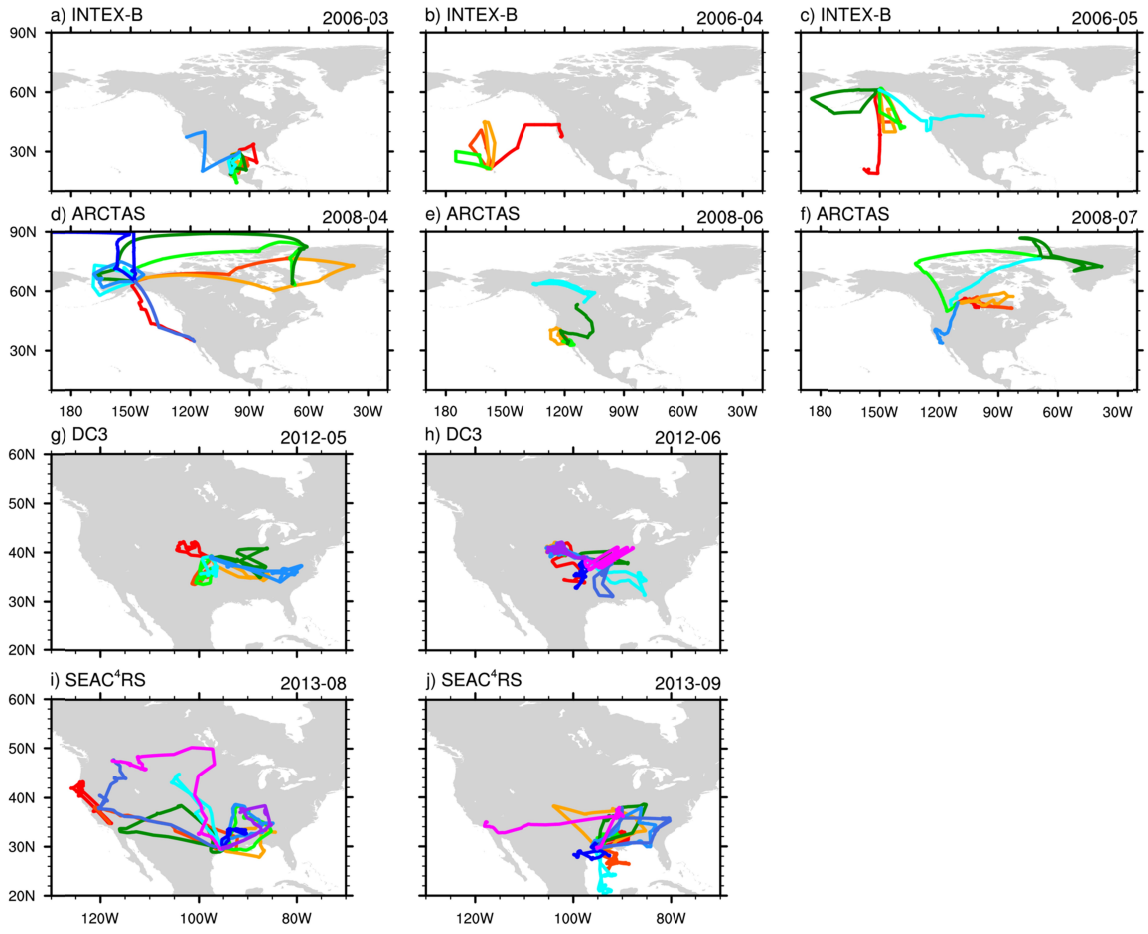

Figure 9. Flight tracks of INTEX-B, ARCTAS, DC3, and SEAC^{4}RS campaigns. The colors represent flight tracks during different days.

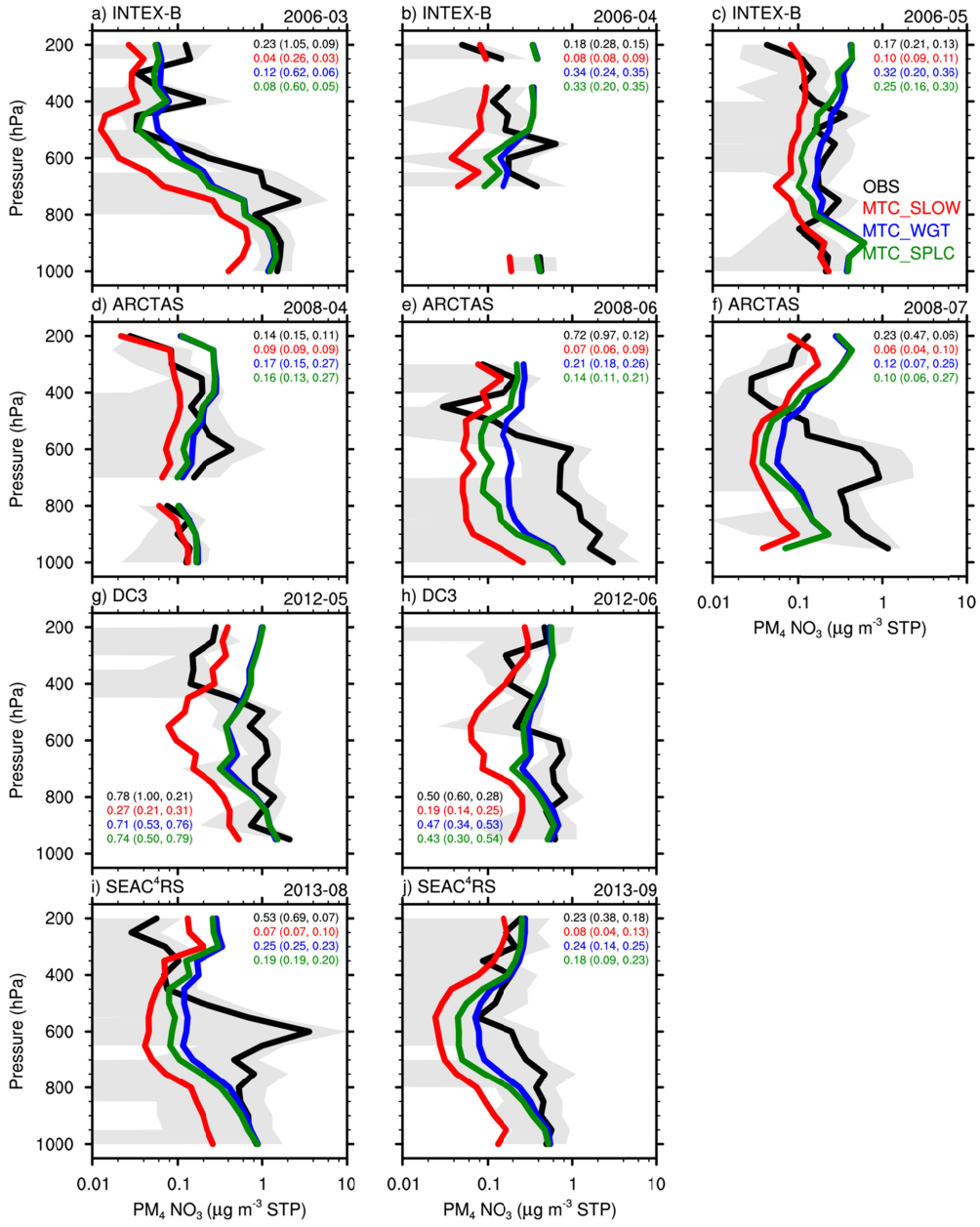

Figure 10. Vertical profiles of nitrate PM_4 mass concentrations (μg m^{-3} in STP) from model simulations (colored lines) and four aircraft campaigns (dark solid lines for mean values in the corresponding month; shaded areas for plus/minus one standard deviation of observations). Numbers shown are median concentrations. Values in parentheses are for

vertical levels below/at and above 500 hPa, respectively.

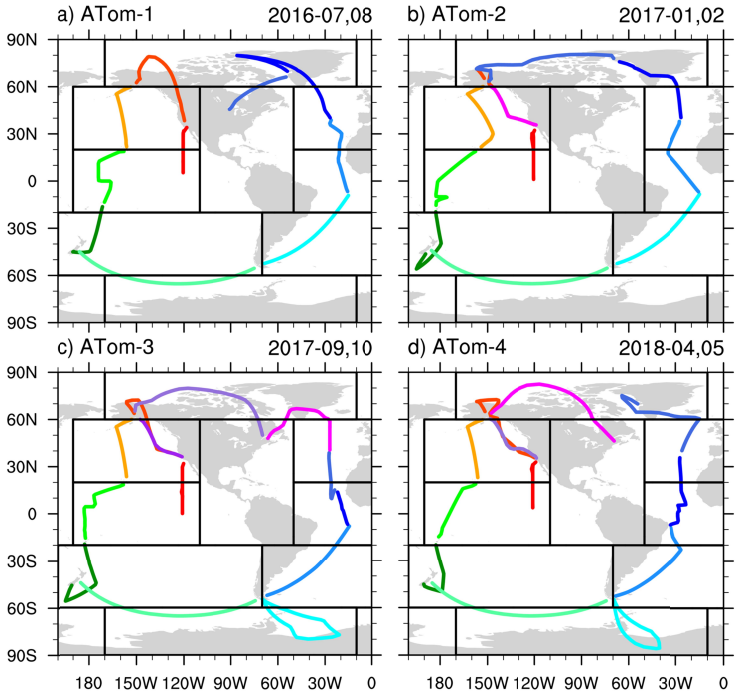

Figure 11. Flight tracks of ATom-1 (Summer, 2016), ATom-2 (Winter, 2017), ATom-3 (Autumn, 2017), and ATom-4 (Spring, 2018) campaigns. Black boxes are regions used for the average of observations and model results along flight tracks. The latitudes and longitudes of these regions are (60ºN-90ºN, 170ºW-10ºW), (20ºN-60ºN, 170ºE-110ºW), (20ºN-60ºN, 50ºW-0º), (20ºS-20ºN, 170ºE-110ºW), (20ºS-20ºN, 50ºW-0º), (60ºS-20ºS, 160ºE-70ºW), (60ºS-20ºS, 70ºW-0º), and (60ºS-90ºS, 170ºW-10ºW). The colors represent flight tracks during different days.

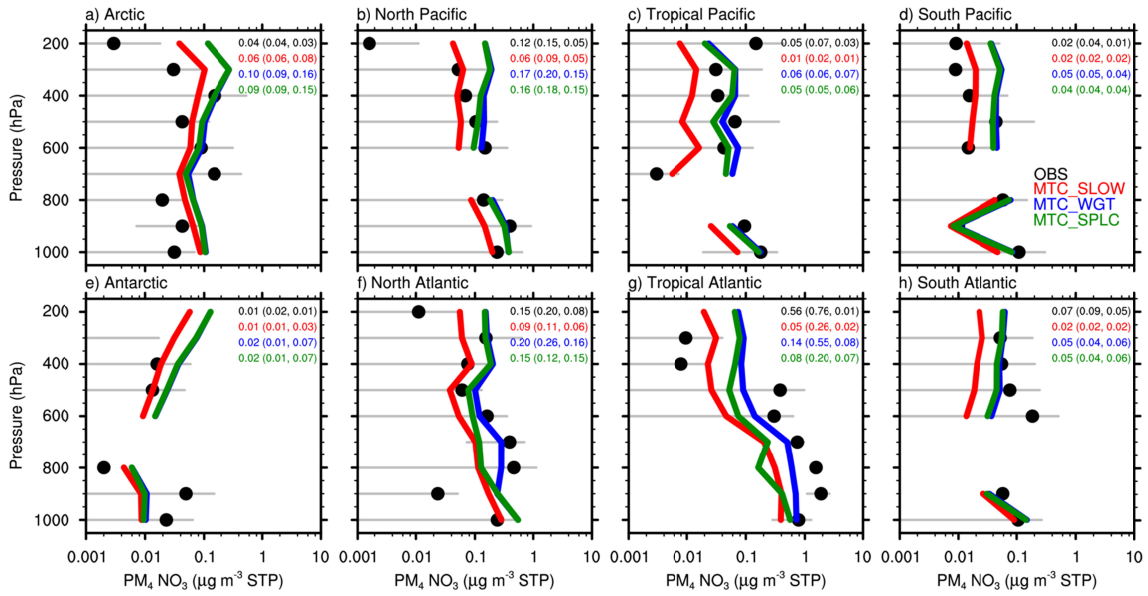

Figure 12. Vertical profiles of nitrate PM_4 mass concentrations (µg m^{-3} in STP) from model simulations (colored lines) and ATom 1-4 campaigns (black dots for mean values; grey lines for plus/minus one standard deviation of observations). Numbers shown are median concentrations. Values in parentheses are for vertical levels below/at and above 500 hPa, respectively.

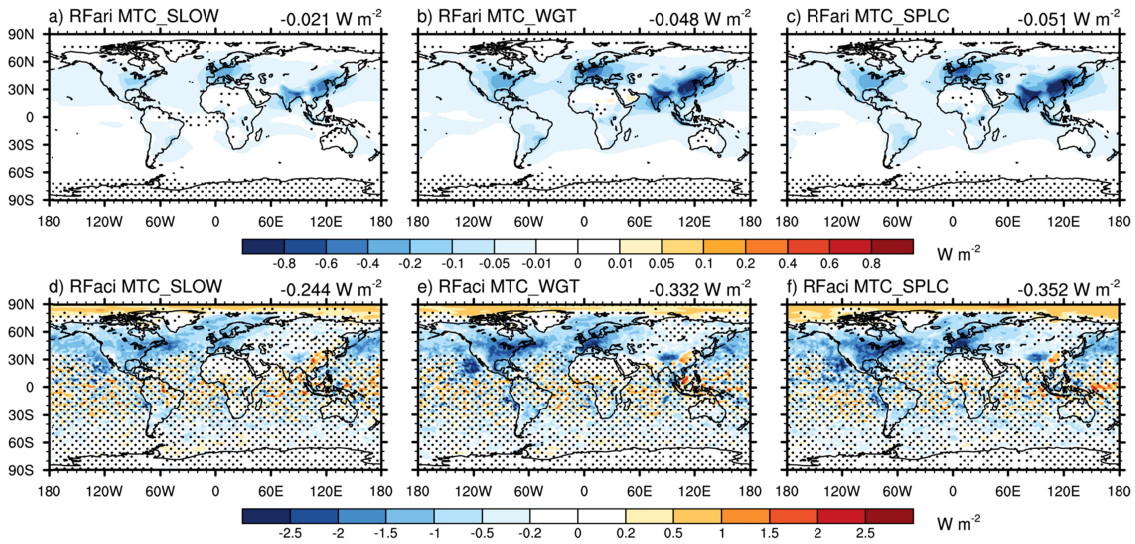

Figure 13. Spatial distributions of RFari (a-c) and RFaci (d-f) of nitrate aerosols between 1850 and 2010. Numbers at the top-right of each panel are global annual mean values. Areas with dots indicate the values with significance level not passing 10%.

1283

1284 **Table 1.** *List of Aerosol Species in the Default and Modified MAM4 Modes*

Species	Accumulation	Aitken	Coarse	Primary carbon
BC	D		D	D
POM	D		D	D
SOA	D	D	D	
MOA	D	D	D	D
SO_4	D	D	D	
NH_4	M	M	M	
NO_3	M	M	M	
Cl	D	D	D	
Na	M	M	M	
Dust	D	M	D	
Ca	M	M	M	
CO_3	M	M	M	
Total	12	10	12	3

1285 Note. "D" indicates species that are present in both default MAM4 and MOSAIC-MAM4.
1286 "M" indicates species added to MOSAIC-MAM4.

1287

1288

1289

1290

1291

1292

1293

1294

1295

1296

1297

1298 **Table 2.** *Summary of Model Experiments with Different Configurations*

Experiment	Aerosol and Precursor Gas Emission	Nitrate Yes/No	Description
Default	2005-2014 (PD)	N	Default setting of E3SMv2
	1850 (PI)	N	
MZT	2005-2014 (PD)	N	E3SMv2 with MOZART gas chemistry
	1850 (PI)	N	
MTC_SLOW	2005-2014 (PD)	Y	MOZART-MAM4-MOSAIC; $\alpha_{HNO_3} \leq 0.0011$ for all aerosol modes in MAM4
	2005-2014 (PD)	N	
	1850 (PI)	Y	
	1850 (PI)	N	
MTC_WGT	2005-2014 (PD)	Y	$\alpha_{HNO_3} \leq 0.0011$ for dust particles; $\alpha_{HNO_3} = 0.193$ for non-dust particles; calculating dust-weighted MTCs for each mode using parameters ($r_{p,m}$, n_m, and α_{HNO_3}) for dust/non-dust particles
	2005-2014 (PD)	N	
	1850 (PI)	Y	
	1850 (PI)	N	
MTC_SPLC	2005-2014 (PD)	Y	same as MTC_WGT in the accumulation and Aitken mode but splitting coarse mode aerosols into the coarse dust and sea salt sub-mode in MOSAIC; $\alpha_{HNO_3} \leq 0.0011$ in the coarse dust sub-mode; $\alpha_{HNO_3} = 0.193$ in the sea salt sub-mode.
	2005-2014 (PD)	N	
	1850 (PI)	Y	
	1850 (PI)	N	
MTC_SPLAC	2005-2014 (PD)	Y	same as MTC_SPLC in the Aitken and coarse mode but splitting accumulation mode aerosols into the fine dust, sea salt and carbon mode in MOSAIC
MTC_FAST	2005-2014 (PD)	Y	same as MTC_SLOW but use $\alpha_{HNO_3} = 0.193$ for all aerosol modes in MAM4

1299

1300

1301

1302

1303

1304

1305

1306

1307 **Table 3.** *Mass Budgets of Nitrate and Ammonium in the Three E3SM Experiments*

NO_3	MTC_SLOW	MTC_WGT	MTC_SPLC
Aqueous Chemistry (Tg N a^{-1})	37.0 (36.9, 0.1)	28.6 (28.5, 0.1)	30.0 (29.9, 0.1)
Gas-aerosol Exchange (Tg N a^{-1})	–24.2 (–30.5, 6.3)	–4.8 (–20.8, 16.0)	–8.9 (–21.7, 12.8)
Gas-aerosol Exchange Production (Tg N a^{-1})	26.8 (20.0, 6.8)	48.5 (29.6, 18.9)	48.6 (32.4, 16.3)
Gas-aerosol Exchange Loss (Tg N a^{-1})	–51.7 (–51.4, –0.3)	–53.9 (–51.5, –2.4)	–57.5 (–54.9, –2.6)
Net Chemistry Production (Tg N a^{-1})	12.8 (6.4, 6.4)	23.8 (7.7, 16.0)	21.1 (8.2, 12.9)
Dry Deposition (Tg N a^{-1})	4.3 (1.1, 3.1)	9.6 (1.7, 8.0)	8.2 (1.7, 6.5)
Wet Deposition (Tg N a^{-1})	8.5 (5.3, 3.3)	14.1 (6.1, 8.1)	12.8 (6.5, 6.4)
Burden (Tg N)	0.096 (0.036, 0.061)	0.237 (0.068, 0.169)	0.185 (0.076, 0.110)
Lifetime (day)	2.75 (2.02, 3.47)	3.64 (3.20, 3.85)	3.21 (3.38, 3.11)
NH_4	MTC_SLOW	MTC_WGT	MTC_SPLC
Aqueous Chemistry (Tg N a^{-1})	8.0	3.7	3.7
Gas-aerosol Exchange (Tg N a^{-1})	8.5	16.1	16.4
Net Chemistry Production (Tg N a^{-1})	16.5	19.8	20.1
Dry Deposition (Tg N a^{-1})	4.4	5.7	5.7
Wet Deposition (Tg N a^{-1})	12.4	14.4	14.7
Burden (Tg N)	0.390 (0.388, 0.003)	0.430 (0.421, 0.009)	0.436 (0.431, 0.006)
Lifetime (day)	8.46	7.80	7.82

1308 Note. Values in parentheses are for the fine (accumulation and Aitken mode) and coarse
1309 mode, respectively.

1310

1311

1312

1313

1314

1315

1316

1317

1318

1319 **Table 4.** *Nitrate Mass Budgets in the Three E3SM Experiments Compared with Other*

1320 *Studies*

	Burden (Tg N)	ChemP (Tg N a^{-1})	Dry Dep (Tg N a^{-1})	Wet Dep (Tg N a^{-1})	Lifetime (day)
MTC_SLOW	0.096 (36.9, 63.1)[a]	12.8 (6.4, 6.4)[b]	4.3	8.5	2.75
MTC_WGT	0.237 (28.7, 71.3)	23.8 (7.7, 16.0)	9.6	14.1	3.64
MTC_SPLC	0.185 (40.9, 59.1)	21.1 (8.2, 12.9)	8.2	12.8	3.21
Bian et al. (2017) (B17)	0.14 [0.03, 0.42][c]	13.7 [1.5, 28.3][d]	4.7 [0.25, 10.8]	10.4 [1.2, 20.5]	5.0 [2.0, 7.8]
	0.15 [0.06, 0.22][e]	13.0 [10.5, 16.2]	4.6 [1.0, 10.5]	10.5 [7.1, 14.2]	4.2 [2.1, 5.9]
Lu et al. (2021) (L21)	0.11 (27.3, 72.7)	12.3 (5.1, 7.1)	2.8	9.3	3.3
	0.135[f]				
Zaveri et al. (2021) (Z21)	0.139	21.7	9.0	12.5	2.36
Xu & Penner (2012) (XP12)	0.17 (52.3, 47.7)[g]	15.9 (8.5, 7.4)	4.0	12.0	3.92
Feng & Penner (2007) (FP07)	0.16 (42.9, 57.1)[g]	11.6 (4.6, 7.1)	3.0	8.6	5.0
Hauglustaine et al. (2014) (H14)	0.18 (27.8, 72.2)	14.4 (3.2, 11.2)	1.7	12.7	4.61

1321 [a]Values in parentheses are mass fractions for the fine (accumulation and Aitken mode)
1322 and coarse modes, respectively. [b]Values in parentheses are net chemistry productions in
1323 the fine and coarse modes, respectively. [c]Values in brackets are minimum and maximum
1324 values, respectively. [d]Values (mean, minimum, and maximum) are summarized from 7
1325 GCMs (9 in total). Only two GCMs directly report chemistry production. The values for
1326 the other five GCMs are obtained from the sum of dry and wet deposition. [e]We select 4
1327 GCMs which simulate the formation of nitrate aerosols in both the fine and coarse modes
1328 and consider the heterogeneous reactions on dust and sea salt particles. [f]The value is from
1329 the experiment coupling MOSAIC and MAM7 in CESM2. [g]Fine mode is for $d_p < 1.25$
1330 μm.

1331

1332

1333

1334

1335

1336

1337

1338

1339 **Table 5.** *RFari and RFaci of Nitrate Aerosols from This Study Compared with Other*

1340 *Studies*

	RFari (W m^{-2})	RFaci (W m^{-2})	Period
MTC_SLOW	–0.021	–0.244	1850-2010
MTC_WGT	–0.048	–0.332	1850-2010
MTC_SPLC	–0.051	–0.352	1850-2010
Lu et al. (2021) (L21)	–0.014	–0.219	1850-2010
Xu & Penner (2012) (XP12)	–0.12	N/A	1850-2010
An et al. (2019) (A19)	–0.14	N/A	1850-2010
Hauglustaine et al. (2014) (H14)	–0.056	N/A	1850-2000
Bellouin et al. (2011) (B11)	–0.12	N/A	1860-2000
Bauer et al. (2007)	–0.06	N/A	1750-2000
Li et al. (2015)	–0.025	N/A	1850-2000
Boucher et al. (2013)	–0.11 (–0.3 to –0.03)	N/A	1750-2010
Myhre et al. (2013)	–0.08 (–0.12 to –0.02)	N/A	1850-2000

1341

1342

1343

1344

1345

1346

1347

1348

1349